Stable bubble formations in a depth-perturbed Hele-Shaw channel

Jack Lawless [1], Jack Keeler [2], Andrew L. Hazel [3] and Anne Juel [1,*]

[1] *Department of Physics and Astronomy, The University of Manchester, Oxford Road, Manchester M13 9PL, United Kingdom*

[2] *School of Mathematics, The University of East Anglia, Norwich Research Park, Norwich NR4 7TJ, United Kingdom*

[3] *Department of Mathematics, University of Manchester, Oxford Road, Manchester M13 9PL, United Kingdom*

(Received 1 March 2024; accepted 3 September 2024; published 25 September 2024)

The propagation of polydisperse bubbles inside a rectangular Hele-Shaw channel by the constant volumetric flux flow of an ambient viscous liquid is generally unsteady; pairs of neighboring bubbles will either separate or coalesce because their propagation speeds increase monotonically with their sizes. Thus, any group of bubbles will eventually rearrange itself in order of decreasing size, individual bubbles will separate, and, crucially, there are no stable multiple-bubble states. Remarkably, the introduction of a small axially uniform elevation to the channel's lower boundary (on the order of a percent of the channel's depth) leads to the creation of stable multiple-bubble states and, thus, disrupts the usual reordering by bubble sizes. The constituent bubbles of such states lie in alternation on opposite sides of the elevation. The elevation provides a mechanism for the trailing bubbles to reduce their propagation speeds when approaching their preceding nearest neighbors. The stable multiple-bubble states are always led by the smallest bubble while the trailing bubbles can be arranged in any order and, thus, their number grows factorially as the number of bubbles increases.

DOI: 10.1103/PhysRevFluids.9.093605

I. INTRODUCTION

Dispersed two-phase flows are found in a variety of natural and industrial processes. The dispersed phase may consist of discrete gas bubbles or liquid droplets that are suspended within a continuous liquid phase [1–3]. The precise dynamics of these flows varies from system to system depending on the confining geometry and fluid properties. However, in general, separation and coalescence are the two prevalent types of long-term behavior between pairs of droplets or bubbles [4–10]. Thus, there are typically no stable multiple-bubble or multiple-droplet states in these flows. Groups of monodisperse bubbles can form neutrally stable, one-dimensional "trains" [10] because they propagate at the same speed and are effectively noninteracting at large distances. However, in general, groups of bubbles in real-world experiments include different bubble sizes which, in turn, propagate at different speeds. In this paper, we explore the transport of multiple bubbles inside a quasi-two-dimensional (Hele-Shaw) channel: a prototypical geometry for studying the nonlinear dynamics of interfaces and their instabilities [11–14]. We show that the introduction of a small

*Contact author: anne.juel@manchester.ac.uk

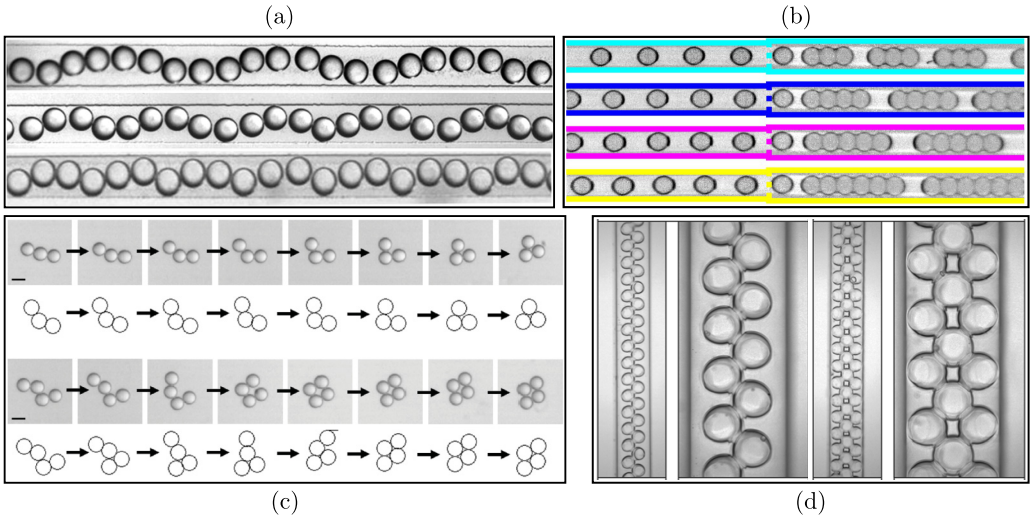

FIG. 1. Examples of groups of microdroplets exhibiting self-organizing dynamics due to controlled geometrical perturbations in a variety of spatially confined (quasi-two-dimensional) channel flows. (a) Transverse vibrational modes that arise in the propagation of a one-dimensional train of monodisperse microdroplets upon exiting a rectangular channel bend. This figure has been adapted from Ref. [17] with permission from the the Royal Society of Chemistry. (b) Trains of monodisperse double-emulsion microdroplets form regularly spaced clusters upon exiting a channel expansion. This figure has been adapted from Schirrmann *et al.* [18] under a Creative Commons license. (c) The self-assembly of monodisperse microdroplets into "building block"-like structures following a steplike increase in the channel's depth. This figure has been adapted from Shen *et al.* [19] under a Creative Commons license. (d) The self-assembly of monodisperse microdroplets into ordered two-dimensional arrays due to an axial gradient in the channel's depth. This figure has been adapted from Ref. [20] with permission from the Royal Society of Chemistry.

elevation along the channel's lower boundary, whose height is on the order of 1% of the channel's depth, suffices to stabilize polydisperse bubble trains and, hence, dramatically increases the number of available steady-state configurations.

Geometrical confinement is widely used to actuate flows in microfluidics, e.g., passive actuation by soft components [15] and flow focusing, which is routinely used in two-phase flows in order to generate large quantities of droplets or bubbles [16]. The introduction of geometric perturbations to the confining geometry can, in turn, promote the self-organization of bubbles and droplets into coherent spatial structures. For example, one-dimensional trains of monodisperse microdroplets were found to exhibit unsteady collective dynamics in the form of longitudinal and transverse vibrational modes when exiting an L-shaped bend as a result of hydrodynamic interactions between neighboring droplets [Fig. 1(a)] [17,21,22]. Furthermore, upon encountering a channel expansion, one-dimensional trains of double-emulsion microdroplets formed regularly spaced clusters through coalescence of their coating films [Fig. 1(b)] [18]. Similarly, groups of microdroplets were found to spontaneously assemble into a variety of complex "building block"-like structures following a steplike increase in the channel's depth [Fig. 1(c)] [19]. The introduction of an axial gradient in the channel's depth profile was shown to promote the self-organization of microdroplets into ordered two- and three-dimensional arrays [Fig. 1(d)] [20]. However, in these examples, the bubbles or droplets are typically monodisperse, stabilized by surfactants, and exhibit little to no deformation because they are sufficiently small that surface tension has the dominant influence on their shapes.

In this paper, we focus on the self-organization of bubbles propagated at finite values of Ca inside a Hele-Shaw channel of large width-to-depth ratio, W^*/H^*, by the constant volumetric flux flow of an ambient viscous liquid. We define the capillary number based on the imposed volumetric

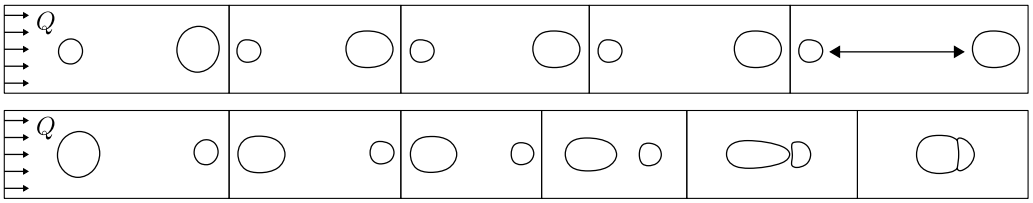

FIG. 2. The typical dynamics of a pair of initially well-separated air bubbles in a horizontally leveled rectangular Hele-Shaw channel of uniform depth when they are subjected to a constant volume flux flow of a surrounding viscous liquid. Time increases from left to right. The channel's width is $W^* = 40.0 \pm 0.1$ mm and its depth is $H^* = 1.0 \pm 0.1$ mm. Top row: The larger bubble is initially situated in the leading position and the two bubbles separate indefinitely along the channel's centerline. Bottom row: The smaller bubble is initially situated in the leading position and the two bubbles aggregate into a cluster. The lubricating film between the bubbles prevents their immediate coalescence. These experiments were performed in the setup that is described in Sec. II A 1 without a centralized elevation.

flux, $\mathrm{Ca} = \mu Q^*/(H^* W^* \sigma)$, where μ is the dynamic viscosity of the surrounding liquid, Q^* is the imposed volumetric flux, and σ is the surface tension at the air-liquid interface. The bubbles inside a Hele-Shaw channel of uniform depth tend to travel steadily along the channel's central axis because of the sidewalls. The extent of a bubble's deformation and its propagation speed relative to the ambient oil flow increase monotonically with Ca and size [11]. Thus, pairs of neighboring bubbles will ultimately either separate or coalesce along the channel's central axis depending on their relative initial positions; the pair of experimental time sequences in Fig. 2 are examples of these two distinct dynamical behaviors. The group of bubbles will, therefore, necessarily rearrange itself into a final configuration that consists of indefinitely separating bubbles arranged in order of decreasing size and there is, crucially, no potential for the existence of steadily propagating multiple-bubble states. A recent Hele-Shaw model of bubble train dynamics in the limit of vanishing capillary number has revealed rich dynamics akin to a Newton's cradle in which neighboring pairs of bubbles successively aggregate and break up as they propagate [23].

We introduce a small, albeit finite, perturbation to the channel's geometry in the form of a centralized elevation along its lower boundary (Fig. 3). The behavior of isolated bubbles has been previously studied extensively in this system, both experimentally [12,14] and numerically [11,24,25], revealing a rich dynamical landscape that arises as a direct consequence of the elevation-induced variation in the channel's depth. For sufficiently large bubbles in an equivalent channel of uniform cross section, a single solution branch is stable for all capillary numbers and it corresponds to the steady, symmetric, and single-tipped family of bubbles (i.e., the finite-size analog of the family of semi-infinite Saffman-Taylor fingers) that are observed in experiments [26]. However, the systematic variation in the channel's depth that is provided by the elevation stabilizes an additional asymmetric solution branch in which the bubble partially overlaps the elevation as it propagates [11,12]. The existence of asymmetric steadily propagating states, importantly, removes the requirement that pairs of bubbles need to be aligned along the channel's centerline and, therefore, they can approach one another from different relative lateral positions. The phenomenon of bubble breakup occurs more readily in the depth-perturbed system because portions of the bubbles can lie in regions of different viscous resistance and, hence, studying the complete evolution of a single bubble generally requires knowledge of the dynamics of multiple bubbles. Thus, driven by a desire to understand the immediate postbreakup behavior, Keeler *et al.* [13] examined the dynamics of two interacting bubbles and, unexpectedly, found a family of stable two-bubble steadily propagating states. The dynamics of larger groups of bubbles was not investigated in that paper but it was hypothesized, based on preliminary experimental observations, that the number of stable multiple-bubble states increases with the number of bubbles.

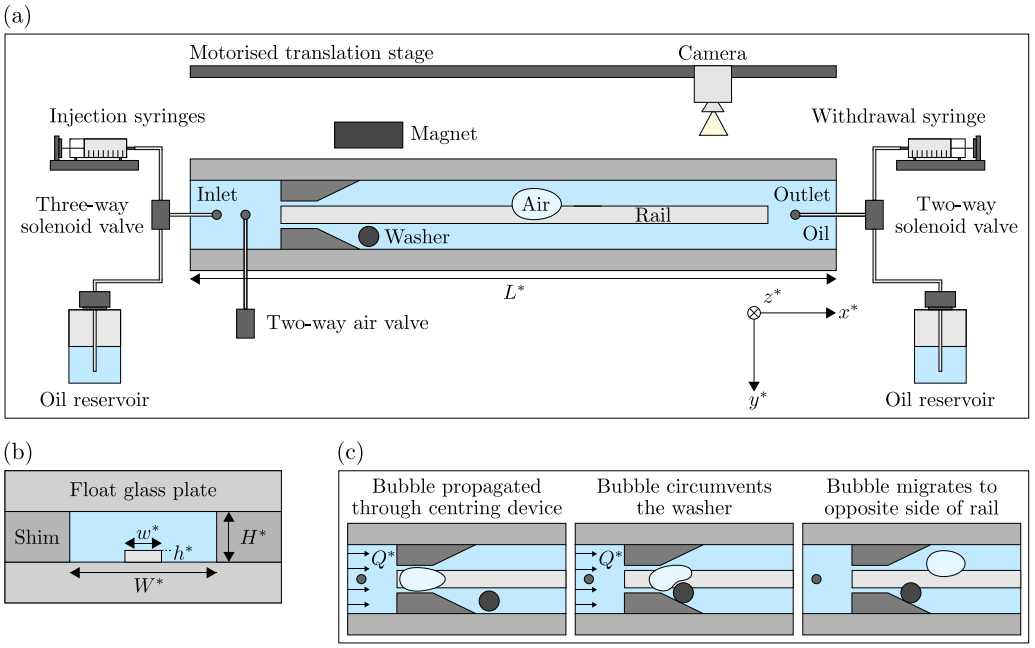

FIG. 3. (a) A schematic diagram of the Hele-Shaw channel that contains a small axially uniform elevation along its centerline. The channel's width is $W^* = 40.0 \pm 0.1$ mm and its depth is $H^* = 1.0 \pm 0.1$ mm. The elevation's width is $w^* = 10.0 \pm 0.1$ mm and its height is $h^* = 24 \pm 1$ μm. The bubbles are generated at the air injection port and are then guided to an asymmetric initial position by constricting the channel with a stainless steel washer. The syringe pumps inject oil into the channel inlet at a constant volumetric flux Q^*. The experiments are recorded in top view by a steadily translating CMOS camera. (b) Cross-section schematic diagram of the channel ($W^* \gg H^*$). (c) A schematic diagram of the procedure that is used to initialize a bubble on a particular side of the elevation.

In the present paper, we examine this hypothesis in detail and identify, through a combination of experiments and numerical simulations, the allowed stable configurations of polydisperse bubbles, henceforth referred to as "formations." The reduced Reynolds number, $\mathrm{Re} = \rho U_b^* H^{*2}/\mu W^*$, where ρ is the density of the liquid, remains small throughout our experiments and, thus, inertial forces are broadly negligible. The physical mechanism that allows the steadily propagating states to occur is identified by sequentially building up the number of bubbles investigated. The presence of the elevated region means that bubble speeds can vary depending on their position within the cross section, which is what enables the stable steadily propagating states to exist. We find that the number of stable multiple-bubble states increases factorially with the number of bubbles. This result is particularly striking because, other than neutrally stable trains of well-separated (i.e., effectively noninteracting) monodisperse bubbles, no similar such states exist inside a Hele-Shaw channel of uniform depth because polydisperse bubbles will always propagate with different speeds. We emphasize that the geometrical perturbation in our system need only occupy a fractional proportion ($<1\%$) of the channel's depth, which is potentially on the scale of the depth resolution of such channels. In other words, a very mild perturbation of the system prevents the natural separation of polydisperse bubble trains and enables large groups of dissimilar bubbles to propagate as a coherent group.

We have organized the paper as follows. The experimental setup and protocols that are implemented in order to reproducibly generate bubbles of prescribed sizes are described in Sec. II A 1. Explaining the origin of the multiple-bubble states relies on a thorough understanding of the behavior of individual bubbles and, thus, we benchmark the propagation of isolated bubbles in

Sec. II A 2. The two-dimensional depth-averaged lubrication model and its numerical implementation are outlined in Sec. II B. We first establish the conditions for which stable steadily propagating formations of two bubbles can occur in Sec. III A by carrying out a series of experiments in which the system's control parameters are varied in order to identify the underlying physical mechanisms. We then build on our acquired understanding of two-bubble formations in order to establish a set of "design principles" for formations with larger numbers of bubbles in Sec. III B and examine their behaviors in response to changes in the system's control parameters. We proceed to discuss the long-term behavior of an arbitrary train of bubbles in Sec. III D and, finally, concluding remarks are made in Sec. IV.

II. METHODS

A. Experimental methods

1. Experimental setup and protocols

The experiments in this study were performed in the same Hele-Shaw channel that was described by Gaillard *et al.* [12], who provide detailed descriptions of both the experimental setup [Fig. 3(a)] and protocols that were implemented in order to reproducibly generate and propagate bubbles of prescribed sizes. Here, we will recall the salient details. The channel consisted of two rectangular float glass plates that were separated by two parallel strips of stainless steel shim [Fig. 3(b)]. The shim's thickness $H^* = 1.00 \pm 0.01$ mm was measured at uniformly spaced points along the channel's length with a micrometer screw gauge and they were separated by a distance $W^* = 40.0 \pm 0.1$ mm with a stainless steel gauge block. The elevation was created by applying a thin strip of translucent PET tape along the centerline of the lower glass plate. The width of the tape was $w^* = 10.0 \pm 0.1$ mm. We performed experiments with two different elevation heights; the majority of experiments that are described in this paper had $h^* = 24 \pm 1$ μm while a smaller number of experiments had $h^* = 10 \pm 1$ μm. Thus, the effective height of the channel in the region above the elevation was reduced by either 2.4% or 1%. The channel was filled with silicone oil (Basildon Chemicals Ltd.) of dynamic viscosity $\mu = 0.019$ Pa s, density $\rho = 951$ kg m^{-3}, and surface tension $\sigma = 21$ mN m^{-1} at the ambient laboratory temperature of $21 \pm 1\,^{\circ}$C. The flow of silicone oil was controlled by a network of three syringe pumps that were connected in parallel. The syringe pumps, channel inlet, and an external oil reservoir were connected by a three-way solenoid valve. The channel outlet and an external oil reservoir were connected by a two-way solenoid valve. Thus, oil could either be driven into the channel at a constant volumetric flux Q^* or withdrawn from the external oil reservoir in order to refill the injection syringes. The injection syringes and solenoid valves were controlled on a computer by a custom-built LabVIEW script.

We generated air bubbles at the air injection port, which was situated a short distance downstream of the channel inlet, by slowly withdrawing a prescribed volume of oil through a syringe that was connected to the channel outlet while the two-way air valve was open to the atmosphere. The bubble was detached and propagated away from the air valve by imposing a small flow of oil. This process was repeated several times in succession in order to generate multiple bubbles of prescribed volumes. The initial separation between the bubbles was controlled by varying the amount of oil that was injected following detachment. The bubbles were then propagated through a "centering device," which consisted of a symmetric channel constriction and a linear expansion region. Upon exiting the centering device, each of the bubbles was guided to an asymmetric initial position by applying an asymmetric constriction to the channel with a magnetic washer [Fig. 3(c)]. The position of the washer was controlled noninvasively by an N52-grade neodymium magnet that was situated underneath the lower glass plate and, by varying the side on which the constriction was applied, the bubbles could be initialized asymmetrically on either side of the elevation.

The bubbles were set into motion by imposing a constant volumetric flux Q^* and filmed in top view by an overhead complementary metal-oxide semiconductor (CMOS) camera, which was mounted onto a motorized translation stage. The camera was programed to translate at a constant

speed, which was selected via an empirical relationship between U_b^* and Q^*, to ensure that the bubbles remained within its field of view throughout the experiment. The observation window of the channel was 1760×330 pixels and, depending on the value of Q^*, the camera's frame rate was varied between 20 and 60. The channel was uniformly illuminated from below by a custom-built LED light box, which led to the air-fluid interface appearing darkened due to light refraction. We used a Canny edge-detection algorithm in order to identify the bubble contours.

We adopt the channel's half-width $W^*/2$ and the mean speed of oil in an equivalent uniform channel $U_0^* = Q^*/W^*H^*$, respectively, as our characteristic length and velocity scales. The capillary number $\mathrm{Ca} = \mu U_0^*/\sigma$ is based on the imposed volumetric flux of oil rather than the bubble's propagation speed, as is typical in related studies. The bubble's propagation speed U_b^* was determined by calculating the streamwise displacement of its center of mass across a series of consecutive frames. The bubble's propagation speed is nondimensionalized based on the mean speed of the ambient oil, $U_b = U_b^*/U_0^*$, and takes values between 1 and 3 in experiments. The bubble's in-plane area A^* was determined from the Canny edge detection algorithm and its size is parametrized in terms of a dimensionless radius $r = 2\sqrt{A^*/\pi}/W^*$.

2. Isolated bubbles

We will primarily work with four bubbles of size $r = 0.33$, $r = 0.40$, $r = 0.47$, and $r = 0.54$ throughout this paper and they will be represented, respectively, by blue, red, green, and purple contours. The general behavior of each bubble when propagated in isolation is benchmarked by showing results for the specific asymmetric states that "combine" to form the stable multiple-bubble state. The bubble's size and the imposed capillary number based on the dimensionless volumetric flux are the two control parameters and their individual influence on the behavior of these (and other) isolated-bubble states has been investigated previously [12,13]. However, the data presented here are new. Movies 1–4 in the Supplemental Material [27] show the typical propagation of the isolated bubbles.

Figure 4(a) shows the dimensionless speed of each isolated bubble as a function of the capillary number and, in each case, the bubble's speed increases sharply from the quasistatic (i.e., $\mathrm{Ca} = 0$) limit and saturates for larger capillary numbers. We note that this behavior is broadly similar to that of a Saffman-Taylor air finger, which is the limiting case as the bubble's size tends to infinity.

Figure 4(b) shows the dimensionless speed of an isolated bubble as a function of its size for several values of Ca. The bubble's dimensionless speed increases monotonically with its size from the tracerlike (i.e., $r = 0$) limit and saturates at $r = r_s \approx 0.90$. For $r \geqslant r_s$, the bubble elongates in the streamwise direction while the in-plane curvature of its front and rear remain unchanged [inset of Fig. 4(b)]. The bubble's speed is determined by the local pressure gradient, which is affected by changes in the viscous dissipation that arise as it displaces the viscous liquid, as well as the surface-tension-induced pressure jump at the interface. The details depend on both the bubble's shape and its location within the channel's nonuniform cross section and we are not aware of any simpler predictive models than numerical solutions of the depth-averaged system that is described in the following section.

The propagating bubbles are surrounded by liquid films on the upper and lower boundaries that have been characterized previously by Gaillard *et al.* [12]. The mean thickness of the liquid films increases as the bubble's propagation speed increases and, for the range of capillary numbers that are investigated in this paper, the mean thickness of the liquid films is larger than the elevation's height.

B. Mathematical model and numerical methods

1. Mathematical model outline

We complement our experiments with numerical simulations of a two-dimensional depth-averaged lubrication model whose validity has been confirmed previously in studies of isolated [12]

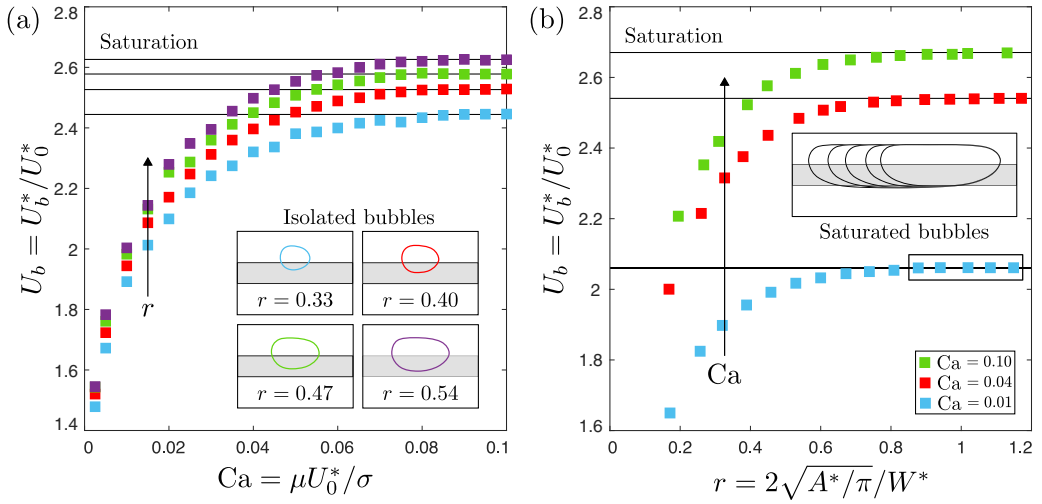

FIG. 4. (a) Variation of the dimensionless bubble speed $U_b = U_b^*/U_0^*$ with the imposed capillary number $\mathrm{Ca} = \mu U_0^*/\sigma$ for isolated asymmetric bubbles of various sizes. Inset: Experimental snapshots of the bubbles at $\mathrm{Ca} = 0.01$. (b) Variation of U_b with the dimensionless bubble size $r = 2\sqrt{A^*/\pi}/W^*$ at three values of Ca that span the investigated range of capillary numbers. Inset: Superimposed experimental snapshots of "saturated" (i.e., $r \geqslant r_s$) bubbles at $\mathrm{Ca} = 0.01$. The bubbles are aligned in the streamwise direction at their tips. The shape of the bubble's front and rear are unchanged for $r \geqslant r_s$. The channel's width is $W^* = 40.0 \pm 0.1$ mm and its depth is $H^* = 1.0 \pm 0.1$ mm. The elevation's width is $w^* = 10.0 \pm 0.1$ mm and its height is $h^* = 24 \pm 1$ μm.

and multiple [13] bubbles. We opt to only describe the model's salient details because its general implementation is unchanged from previous studies. The truncated dimensionless computational domain and its cross section are shown in Fig. 5. The elevation is modeled by a piecewise-smooth depth profile $b(y)$ of the form

$$b(y) = 1 - \frac{h}{2}[\tanh(s(y+w)) - \tanh(s(y-w))], \tag{1}$$

where $h = 0.024$ is the dimensionless height and $w = 0.25$ is the dimensionless width of the elevation in accordance with experiments. The parameter $s = 40$ determines the sharpness of the elevation's edges [24]. We perform our simulations in a comoving frame of reference that translates

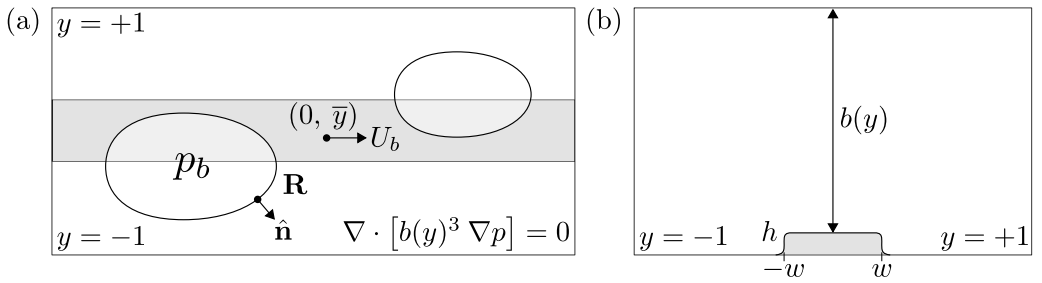

FIG. 5. (a) The truncated dimensionless computational domain. The bubbles have constant internal pressures. The bulk flow is governed by a two-dimensional depth-averaged lubrication equation [Eq. (2)]. The streamwise component of the bubbles' center of mass is constrained to remain fixed at zero. (b) Cross-section diagram of the computational domain. The variable channel depth is modeled by a piecewise-smooth depth profile $b(y)$ [Eq. (1)].

with velocity $\mathbf{U}(t) = (U_b(t),\ 0)$, where $U_b(t)$ is an unknown of the problem that is obtained by requiring that the streamwise component of the center of mass of the group of bubbles is fixed at zero. Upon applying lubrication theory [28] and depth averaging, the three-dimensional Navier-Stokes equations in the fluid domain reduce to a single two-dimensional lubrication equation in terms of the dimensionless fluid pressure p,

$$\boldsymbol{\nabla} \cdot [(b(y)^3\ \boldsymbol{\nabla} p] = 0. \tag{2}$$

We impose no-penetration conditions on the channel sidewalls, i.e., $p_y = 0$ at $y = \pm 1$. We denote the coordinates of a point on the air-fluid interface by $\mathbf{R}$ and impose a no-penetration condition:

$$\frac{\partial \mathbf{R}}{\partial t} \cdot \hat{\mathbf{n}} = [-b(y)^2\ \boldsymbol{\nabla} p - \mathbf{U}(t)] \cdot \hat{\mathbf{n}}, \tag{3}$$

where $\hat{\mathbf{n}}$ is the outward-pointing unit normal vector to the interface at $\mathbf{R}$. The pressure jump across the interface, arising exclusively due to surface tension, is described by the Young-Laplace equation:

$$[[p]]^{\text{bubble}}_{\text{fluid}} = \frac{1}{3\alpha Q}\left[\frac{\kappa}{\alpha} + \frac{1}{b(y)}\right], \tag{4}$$

where the dimensionless in-plane curvature of the interface at $\mathbf{R}$ is denoted by κ. The transverse curvature term $1/b(y)$ assumes that the bubble occupies the entirety of the channel depth and the interface is semicircular with radius of curvature $b(y)/2$. The (constant) internal pressure of each bubble is determined by requiring that their dimensionless volumes remain constant. The mathematical model does not allow for imposition of tangential stress or tangential velocity boundary conditions nor does it incorporate the presence of liquid films around the bubbles on the upper and lower channel boundaries. However, as in previous studies, we find that the model qualitatively captures all of the dynamics that are observed in experiments. There is a quantitative discrepancy in the values of Ca at which particular phenomena occur between experiments and numerical simulations. This discrepancy increases as Ca is increased and we believe that this is primarily driven by the corresponding increase in the thickness of the neglected liquid films in experiments. We will discuss this issue further in Sec. III A.

The system was spatially discretized by using a finite element method in the open-source library `oomph-lib` [29]. We propagated elliptical bubbles from specified initial placements in the computational domain by imposing a constant pressure gradient in the streamwise direction. The value of the pressure gradient was chosen in order to obtain a specified capillary number Ca based on the imposed volumetric flux of the ambient fluid. The bubbles were initialized sufficiently far apart in order to prevent their immediate aggregation following the imposition of flow. The temporal evolution of the bubbles was simulated by employing a backwards difference time-stepping algorithm (BDF2) with a time step $\Delta t = 0.01$. For brevity, we have omitted information relating to the handling of the finite element mesh (see Ref. [12] for details) but confirm that all of the presented numerical results are fully resolved.

2. Isolated bubbles

The bubble's nondimensional speed in the depth-averaged lubrication model exhibits broadly similar behaviors to those in experiments and, for brevity, we have not included the corresponding plots. We can use the numerical simulations in order to quantify the flow field perturbations that are imposed by the asymmetrically propagating bubbles. The single-phase flow field (i.e., in the absence of a bubble) $U = U(y)$ is shown in Fig. 6(a). The ambient fluid's dimensionless speed $U = |\mathbf{u}|$ is given by $U = 0.97$ and $U = 1.02$ in the occluded and unoccluded regions, respectively, sufficiently far away from the elevation's edges. The small decrease in the ambient fluid's speed in the occluded region is a consequence of the local increase in the channel's viscous resistance. The mathematical model does not allow for imposition of the no-slip condition on the channel sidewalls and, hence, there are no boundary layers in these regions. However, in general, the effects of this simplification are insignificant because the bubbles propagate sufficiently far away from the channel's sidewalls.

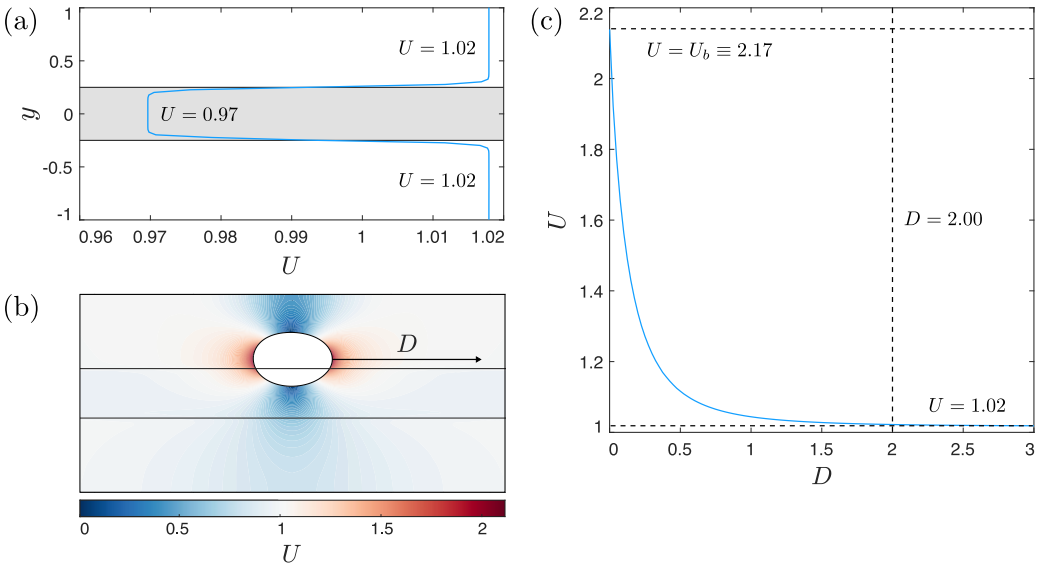

FIG. 6. (a) Variation of the dimensionless fluid speed $U = |\mathbf{u}|$ with y in a channel without a bubble at $\mathrm{Ca} = \mu U_0^*/\sigma = 0.04$ in the depth-averaged lubrication model. (b) The flow field in the vicinity of an isolated bubble of size $r = 0.33$ at $\mathrm{Ca} = 0.04$ in the depth-averaged lubrication model. The dimensionless fluid speed is represented by the heat map. (c) Variation of $U = |\mathbf{u}|$ with the dimensionless streamwise distance $D = 2D^*/W^*$ from the bubble's tip.

The localized perturbation that is imposed by the propagation of an isolated bubble onto the surrounding flow field is shown in Fig. 6(b). The fluid's speed U is represented by the heat map; blue regions correspond to $U < 1$ and red regions correspond to $U > 1$. The speed of the ambient fluid increases in the vicinity of the bubble's front and rear while it decreases in the vicinity of its sides. The sharp decay of the flow field perturbation with increasing distance is evident in Fig. 6(c), where U is plotted as a function of the dimensionless streamwise distance $D = 2D^*/W^*$ from the bubble's tip. The ambient fluid's speed at the bubble's tip is equal to U_b as a consequence of Eq. (3) and the far-field fluid speed is reattained (within 0.5%) at $D = 2$. However, the decay rate of the flow field perturbation is slower than that predicted by simple dipole models that are used to model small bubbles in Hele-Shaw channels [30] and this indicates that these bubbles are in a regime in which finite-size effects are important.

III. RESULTS

A. Stable two-bubble formations

We begin by characterizing the fundamental physical features of the stable formations of two bubbles that were identified by Keeler *et al.* [13]. The experimental time sequence in Fig. 7(a) is a typical example of two bubbles organizing into a stable formation when propagated from rest on opposite sides of the elevation. The leading bubble's size is $r_1 = 0.33$, the trailing bubble's size is $r_2 = 0.40$, and the dimensionless flow rate is $Q = \mu U_0^*/\sigma = 0.01$. Thus, in the absence of any interaction, the trailing bubble would propagate faster than the leading bubble (see Sec. II A 2). Furthermore, if the two bubbles were located on the same side of the elevation, or if there were no elevation, the trailing bubble would eventually catch up to the leading bubble and form an aggregate. However, the barrier between bubbles that is presented by the elevation provides enough additional resistance to prevent their aggregation and, instead, the bubbles preserve their initial order following the imposition of flow and evolve transiently until their shapes and separation do not change with

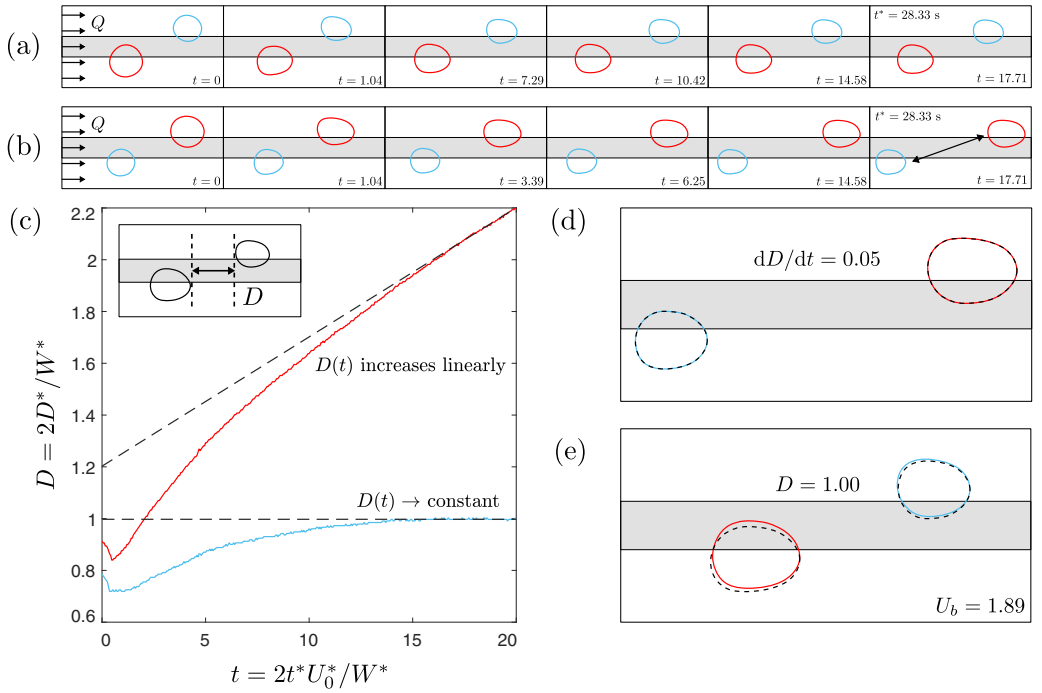

FIG. 7. [(a), (b)] Experimental time sequences of two bubbles of size $r = 0.33$ and $r = 0.40$ when propagated from rest on opposite sides of the elevation at $\mathrm{Ca} = \mu U_0^*/\sigma = 0.01$. The smaller bubble is initially situated in the leading position in (a) while the larger bubble is initially situated in the leading position in (b). (c) The corresponding time evolutions of the dimensionless separation $D = 2D^*/W^*$ between the two bubbles. [(d), (e)] Superposition of the final bubble shapes with their corresponding isolated bubbles (dashed black contours). The leading bubble's shape does not change while the trailing bubble broadens and increases its overlap of the elevation.

time. This behavior is reflected in the temporal evolution of the dimensionless streamwise separation $D = 2D^*/W^*$ between the trailing bubble's front and the leading bubble's rear [Fig. 7(c)]. The separation between the two bubbles in their stable formation is $D = 1.00$ and its speed $U_b = 1.89$ is equal to the leading bubble's isolated speed. However, upon reversing the order of the two bubbles in Fig. 7(b), because the trailing bubble propagates more slowly than the leading bubble, they proceed to separate indefinitely. The gradient of D (i.e., the rate at which the two bubbles separate over time) decreases monotonically and tends towards a constant value $\mathrm{d}D/\mathrm{d}t = 0.05$ for $D > 2$ and this is equal to the difference between the speeds of the two corresponding steadily propagating isolated bubbles. Movies 5 and 6 in the Supplemental Material [27] show the evolution of the bubbles in both initial configurations.

We have superimposed the shapes of these isolated bubbles (dashed black contours) onto the final panels. The two separating bubbles adopt identical shapes to their isolated counterparts for $D > 2$ because they are effectively noninteracting [Fig. 7(d)]. However, the two bubbles adopt different shapes in their stable formation [Fig. 7(e)]. The shape of the leading bubble's front does not change but its rear inclines modestly away from the channel's centerline. By contrast, the trailing bubble changes shape significantly because it increases its overlap of the elevation and broadens. The changes in the shape and position of the trailing bubble are accompanied by a reduction in its propagation speed to that of the leading bubble. The geometric remodeling of the trailing bubble and, thus, the resulting decrease in its propagation speed is what allows the stable formation of bubbles to exist.

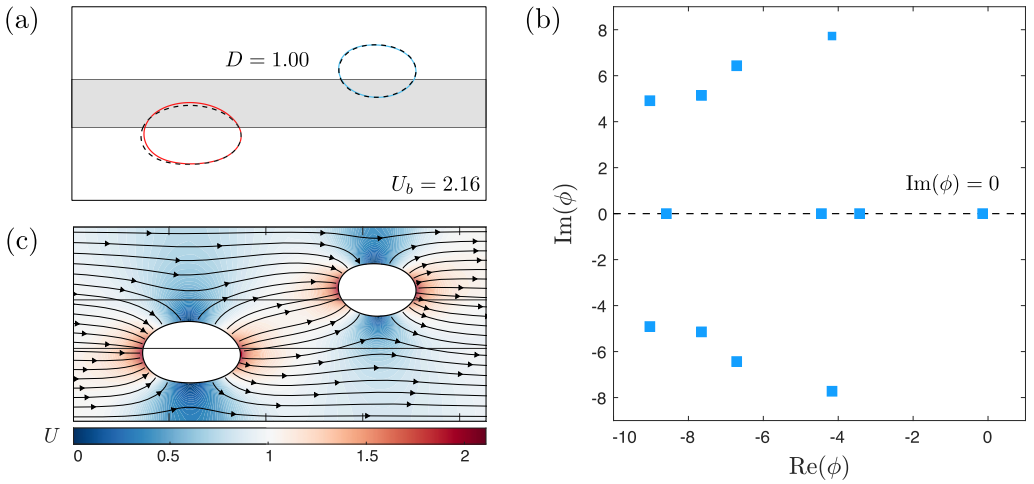

FIG. 8. (a) A stable formation of two bubbles that was obtained from a numerical simulation of the depth-averaged lubrication model at $\mathrm{Ca} = \mu U_0^*/\sigma = 0.04$. The two bubbles have sizes $r_1 = 0.33$ and $r_2 = 0.40$. The overlaid dashed black contours are the corresponding isolated bubble shapes; the leading bubble's shape does not change while the trailing bubble broadens and increases its overlap of the elevation. The formation's speed $U_b = 2.16$ is marginally (<1%) slower than the leading bubble's isolated speed $U_b = 2.17$. (b) The formation's 12 least-stable eigenvalues that were obtained from a linear stability analysis. The set of eigenvalues consists of negative real eigenvalues and complex conjugate eigenvalues with negative real parts and, therefore, the formation is stable. (c) Streamlines of the fluid flow in the laboratory frame of reference and heat map of the dimensionless fluid speed $U = U^*/U_0^*$ in the vicinity of the bubbles.

We find qualitatively similar behavior in numerical simulations of the depth-averaged lubrication model but, as discussed previously, there is a quantitative disagreement between experiments and numerical simulations. The bubbles have different shapes and propagate at slower speeds in numerical simulations compared to experiments at equal capillary numbers and this is mainly a consequence of neglecting the presence of liquid films on the upper and lower channel boundaries. The system is driven by a constant volume flux of the liquid and the air bubble displaces the liquid as it propagates. When liquid films are present, the air bubble displaces less liquid and, therefore, it must propagate at a faster speed to achieve the same overall volumetric flux. Although it is possible to include the effects of liquid films into the depth-averaged model (see, for example, Refs. [31,32]), this requires knowledge of the film thickness as a function of Ca and also the bubble position within the channel, which, as far as we know, can only be predicted by three-dimensional simulations. It is also possible to incorporate tangential boundary conditions at the interface and walls of the channel, but not without the introduction of higher-derivative terms into the governing equations, e.g., the Brinkman equations, as described in Refs. [33–35] in the context of Hele-Shaw cells.

There are several considerations that could be made in regards to choosing the "most suitable" capillary number in numerical simulations when taking into account the known quantitative discrepancies. We opted to keep the bubble sizes the same as in experiments and adjusted the capillary number until the same separation ($D = 1.00$) was obtained between the bubbles. The same separation between the bubbles was obtained at $\mathrm{Ca} = 0.04$ and Fig. 8(a) shows the numerically computed formation of two bubbles. The formation's stability was determined by carrying out a linear stability analysis using the same approach described in detail by Thompson *et al.* [24] and summarized in the Appendix. For the two-bubble system, the 12 least-stable eigenvalues are plotted in Fig. 8(b), where a combination of real, negative eigenvalues and complex conjugate eigenvalues with negative real components indicates that the state is stable. The numerical model captures all of the formation's qualitative characteristics that were identified in experiments. For

example, the formation's speed $U_b = 2.16$ is marginally (<1%) slower than the leading bubble's isolated speed $U_b = 2.17$. However, the formation's speed and the bubble shapes differ significantly from those in experiments. We have overlaid the corresponding isolated bubble shapes (dashed black contours) onto the stable two-bubble formation in Fig. 8(a). The leading bubble's shape is visibly unchanged from its isolated counterpart, whereas the trailing bubble broadens and increases its overlap of the elevation (albeit by a smaller amount than in experiments). The heat map shows that the flow field ahead of the leading bubble is unaffected by the flow field perturbation that is imposed by the trailing bubble [Fig. 8(c)]. However, the two bubbles form an adjoined flow field perturbation in the region between the leading bubble's rear and the trailing bubble's front because the bubbles are within their characteristic interaction range [Fig. 6(c)].

We have obtained a similar qualitative agreement for a variety of different capillary numbers and bubble sizes and, having thus established a broad qualitative agreement between the experiments and mathematical model, we will now proceed to explore the effects of key parameter variations on the behavior of a stable formation of two bubbles.

1. Variation of the trailing bubble's size

The experimental snapshots in Figs. 9(a)–9(c) show the stable formation of two bubbles as the size of the trailing bubble r_2 is increased while the leading bubble's size $r_1 = 0.33$ and capillary number $\mathrm{Ca} = 0.04$ are fixed. Remarkably, the leading bubble's shape is hardly affected by the change in the trailing bubble's size. The shape of the leading bubble's front does not change because this region of the flow field is unaffected by the flow field perturbation that is imposed by the trailing bubble [Fig. 8(c)]. However, its rear inclines away from the channel's centerline slightly as the trailing bubble's size increases. The slight inclination of the leading bubble's rear does not change its propagation speed and, thus, the stable formation's propagation speed ($U_b = 1.89$) is constant for all values of r_2.

The separation $D = 2D^*/W^*$ between the bubbles decreases monotonically as the trailing bubble's size is increased [Fig. 9(d)] because the trailing bubble's isolated speed increases [Fig. 4(b)]. Thus, the reduction in the trailing bubble's speed ΔU_b that is required in order for it to match the leading bubble's speed also increases monotonically with r_2 [Fig. 9(e)]. The increasing speed reduction that is needed for the bubbles to propagate in a stable formation requires an increasingly significant perturbation to the trailing bubble's shape and this is achieved by it moving closer to the leading bubble's rear so that it experiences a local pressure perturbation of increased magnitude. The linear variation of D with ΔU_b on a log-log scale indicates an approximate power-law relationship over a limited range of parameters [see inset of Fig. 9(e)]. Eventually, the separation between the bubbles saturates at a minimum value $D = D_{\min} \equiv 0.72$ for $r_2 \geqslant r_s$ because the speed of the trailing bubble reaches a maximum value (i.e., the limit of a semi-infinite Saffman-Taylor finger) and, thus, ΔU_b saturates at a maximum value $\Delta U_b = \Delta U_{b\max} \equiv 0.15$. The separation between the bubbles increases sharply in the limit $r_2 \to r_1$ because the bubbles will propagate at the same speed when their sizes are equal and, therefore, $\Delta U_b \to 0$. This is the so-called degenerate case that is preserved in a Hele-Shaw channel of uniform depth.

The trailing bubble's shape becomes increasingly perturbed (relative to that of its isolated state) as its size increases because a greater reduction in its speed and, therefore, a more significant geometrical remodeling is required in order for it to match the speed of the leading bubble. There are two different mechanisms by which reconfiguration of the trailing bubble can lead to a change in its speed because its width and/or position within the channel's cross section can change. The maximum width of the trailing bubble's cross section, $\lambda = 2\lambda^*/W^*$, and the proportion of its cross section that overlaps the elevation, $\lambda_{\mathrm{overlap}} = 2\lambda_{\mathrm{overlap}}/W^*$ [defined in Fig. 9(a)], progressively increase and, in doing so, deviate increasingly from their isolated counterparts as r_2 increases [Fig. 9(f)]. The trailing bubble fully overlaps the elevation at $r_2 = 0.62$ (i.e., when $\lambda_{\mathrm{overlap}} = 0.50$) and continues to broaden thereafter. However, the trailing bubble's speed continues to decrease after it fully overlaps the elevation. This behavior indicates that the reduction in the trailing bubble's

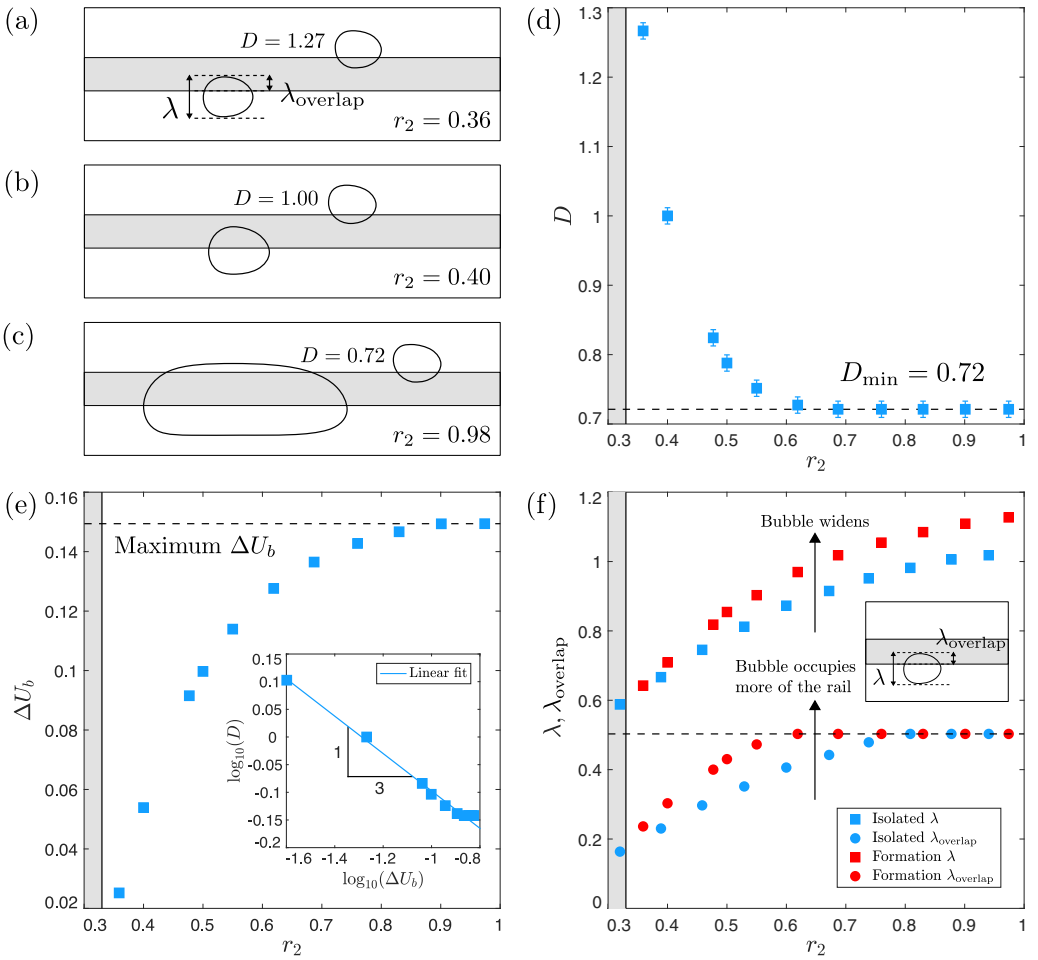

FIG. 9. [(a)–(c)] Experimental snapshots of stable two-bubble formations as the middle bubble's size r_2 increases. The leading bubble's size $r_1 = 0.33$ and the capillary number $\text{Ca} = \mu U_0^*/\sigma = 0.04$ are fixed. (d) Variation of the streamwise separation between the leading bubble's rear and the trailing bubble's front, $D = 2D^*/W^*$, with r_2. (e) Variation of the difference between the two isolated bubble speeds ΔU_b with r_2. Inset: Log-log plot of D versus ΔU_b. The linear fit indicates that the two quantities are related by a power-law relationship over the investigated range of parameters. (f) Variation of the maximum width of the trailing bubble's cross section, $\lambda = 2\lambda^*/W^*$, and the trailing bubble's maximum overlap of the elevation, $\lambda_{\text{overlap}} = 2\lambda^*_{\text{overlap}}/W^*$, with r_2. The two quantities deviate increasingly from their isolated counterparts as the trailing bubble's size increases. Error bars have been omitted in (e) and (f) because they are smaller than the data markers.

speed is achieved by a complex interplay between the variation in its overlap of the elevation (i.e., position within the channel's cross section) and width (i.e., shape).

2. Variation of the capillary number

The experimental snapshots in Figs. 10(a)–10(c) show the stable formation of two bubbles as the capillary number $\text{Ca} = \mu U_0^*/\sigma$ is increased while the leading bubble's size $r_1 = 0.33$ and trailing bubble's size $r_2 = 0.40$ are fixed. The formation propagates at the leading bubble's isolated speed [Fig. 10(d)] and the leading bubble's shape is largely identical to its isolated counterpart in all

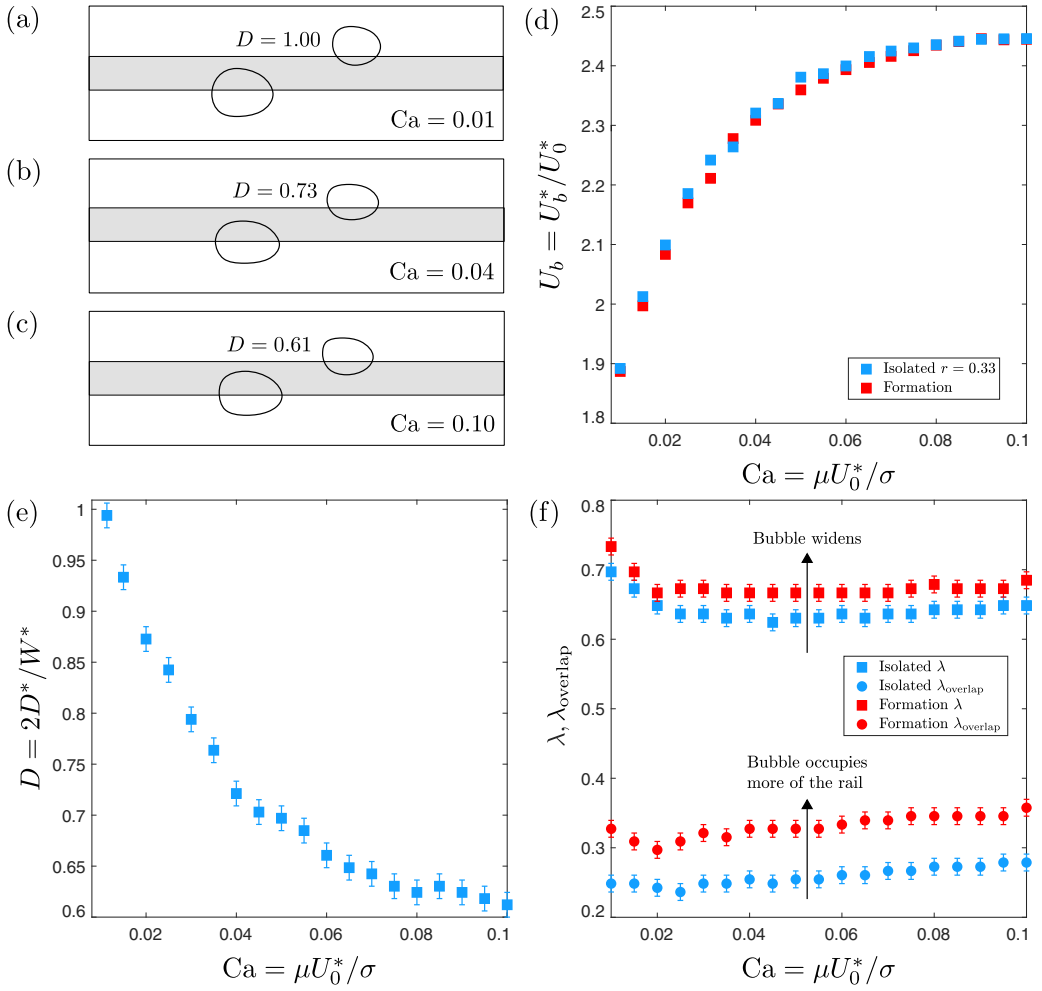

FIG. 10. [(a)–(c)] Experimental snapshots of stable two-bubble formations as the imposed capillary number $\text{Ca} = \mu U_0^*/\sigma$ increases. The leading bubble's size $r_1 = 0.33$ and the trailing bubble's size $r_2 = 0.40$ are fixed. [(d), (e)] Variation of the bubble's speed relative to the surrounding liquid's mean speed $U_b = U_b^*/U_0^*$ with Ca. (e) Variation of the streamwise separation between the leading bubble's rear and the trailing bubble's front, $D = 2D^*/W^*$, with Ca. (f) Variation of the maximum width of the trailing bubble's cross section $\lambda = 2\lambda^*/W^*$ and the trailing bubble's maximum overlap of the elevation, $\lambda_{\text{overlap}} = 2\lambda_{\text{overlap}}/W^*$, with Ca. Error bars have been omitted in (d) because they are smaller than the data markers.

cases. However, the bubbles' shapes become increasingly slender as the capillary number increases because of the increasing influence of viscous forces.

The separation $D = 2D^*/W^*$ between the bubbles decreases monotonically as the capillary number is increased from the quasistatic (Ca = 0) limit [Fig. 10(e)]. The experiments described in Sec. III A 1 indicated that the separation between the bubbles at a fixed capillary number is primarily dictated by the required reduction in the trailing bubble's speed and, therefore, the difference between their isolated speeds, ΔU_b. However, in this case, ΔU_b barely changes because, although both of the individual bubbles' isolated speeds increase, they increase by approximately the same amount [Fig. 4(a)]. Thus, the trailing bubble's maximum width and its overlap of the elevation both increase by an approximately constant value (i.e., the two corresponding curves are translations)

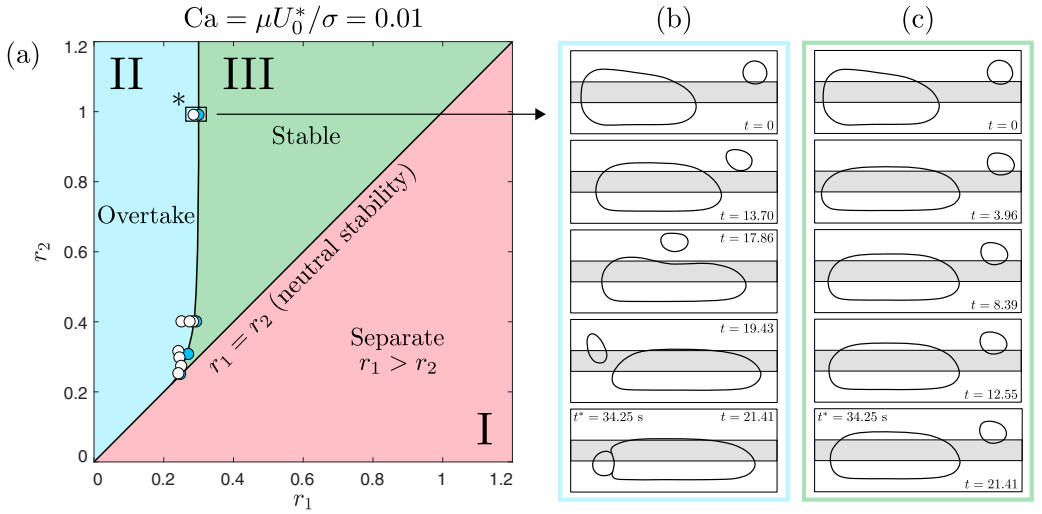

FIG. 11. (a) Two-dimensional phase diagram that classifies the long-term behavior of two bubbles initialized on opposite sides of the elevation when propagated from rest at Ca $= \mu U_0^*/\sigma = 0.01$. The channel's width is $W^* = 40.0 \pm 0.1$ mm and its depth is $H^* = 1.0 \pm 0.1$ mm. The elevation's width is $w^* = 10.0 \pm 0.1$ mm and its height is $h^* = 24 \pm 1$ μm. The leading bubble has size r_1 and the trailing bubble has size r_2. The solid blue markers correspond to the bubbles organizing into a stable formation, whereas the solid white markers correspond to an overtaking of the leading bubble by the trailing bubble. [(b), (c)] Experimental time sequences of two bubbles when propagated from rest at Ca $= 0.01$ while the trailing bubble's size is fixed at $r_2 = 1.00$. The leading bubble's size is $r_1 = 0.29$ in (b) and $r_1 = 0.30$ in (c).

as Ca increases [Fig. 10(f)] because the same reduction in its propagation speed requires a similar degree of geometric remodeling. We, therefore, attribute the decrease in the separation between the bubbles with increasing capillary number to the decreasing significance of the flow field perturbation that is induced by the leading bubble relative to the background pressure gradient because the trailing bubble needs to move closer to the leading bubble in order to experience the required flow field perturbation that results in its necessary geometric change.

3. Two-bubble phase diagram

The two-dimensional phase diagram in Fig. 11(a) classifies the long-term behavior of pairs of bubbles (r_1, r_2) when propagated from rest on opposite sides of the elevation at a fixed value of the capillary number Ca $= \mu U_0^*/\sigma = 0.01$. We note that it is qualitatively representative of all capillary numbers that were investigated. The bubbles were initialized sufficiently far apart in order to prevent their immediate aggregation following the imposition of flow. We find that their long-term behaviors are grouped into three simply connected regions, denoted by I, II, and III, which are described as follows.

Within region I, where $r_1 > r_2$, the trailing bubble's isolated speed is less than that of the leading bubble. There is no mechanism that can slow down the leading bubble or speed up the trailing bubble in this case and, thus, the two bubbles separate indefinitely. The two bubbles ultimately propagate independently because they do not feel the flow field perturbation that is imposed by the other bubble at sufficiently large ($D > 2$) separations.

Within region II, where $r_1 < r_2$, the two bubbles do not organize into a stable formation and, instead, the trailing bubble overtakes the leading bubble. In this case, the flow field perturbation that is imposed by the leading bubble is too small to provoke the geometric changes that are required in the trailing bubble in order to reduce its speed to that of the leading bubble.

Within region III, where $r_1 < r_2$, the two bubbles organize into a stable formation because the flow field perturbation that is imposed by the leading bubble is able to remodel the trailing bubble sufficiently and, consequently, reduce its speed to that of the leading bubble. A stable two-bubble formation exists for all $0.30 \leqslant r_1 < r_2$. However, a stable formation only exists within a limited interval of r_2 for $0.24 \leqslant r_1 \leqslant 0.29$ and the size of the interval decreases as r_1 decreases. We were unable to resolve any stable formations for $r_1 < 0.24$.

The pair of experimental time sequences in Figs. 11(b) and 11(c) shows the dynamical transition between regions II and III for $r_2 = 1.00$ (highlighted on the phase diagram). The trailing bubble overtakes the leading bubble in Fig. 11(b) for $r_1 = 0.29$, whereas the two bubbles organize into a stable formation in Fig. 11(c) for $r_1 = 0.30$. In the former case, the two bubbles aggregate and form a compound bubble whose propagation speed is equal to that of an isolated bubble of size $\sqrt{r_1^2 + r_2^2}$ [12]. The compound bubble only exists transiently because fluid is expelled from the lubrication film until it ruptures at a critical thickness and this ultimately results in their coalescence. However, more time (and, therefore, a longer channel) would be required in order to observe this phenomenon in experiments. We do not have a completely rigorous explanation as to why the crossover between the two long-term behaviors occurs at $r_1 \approx 0.30$. However, it is clear that the leading bubble would inevitably be overtaken by the trailing bubble in the tracerlike limit ($r_1 \to 0$) because the leading bubble will move passively with the flow and, therefore, not perturb the surrounding flow field or the trailing bubble's shape. The extent of the leading bubble's flow field perturbation increases with its size. Figure 4(b) shows that for $\mathrm{Ca} = 0.01$, the trailing bubble's speed and tip shape saturate and become independent of r_2 for $r_2 \geqslant 0.90$, which then explains why the crossover eventually becomes independent of r_2: the leading bubble's perturbation will have the same effect on the trailing bubble's tip and, therefore, its speed once the speed has saturated. For smaller values of r_2, Fig. 4(b) also shows that the rate of change of bubble speed with its radius increases, suggesting that a less significant perturbation would be required to slow down the bubble; i.e., the system will become stable at a smaller value of r_1, as is observed.

We summarize our findings of steadily propagating two-bubble states as follows. The bubbles have to be located on opposite sides of the elevation and the leading bubble must be smaller (and, therefore, slower) than the trailing bubble. However, the leading bubble must also be sufficiently large such that its local perturbation to the flow field is sufficient to cause the required deformation of the trailing bubble that reduces its speed to match that of the leading bubble.

B. Stable three-bubble formations

1. Variation of the bubble order

We will now proceed to build on our understanding of stable two-bubble formations and explore the stability of larger groups of bubbles. There are $3! = 6$ distinct initial arrangements of three bubbles lying in alternation on opposite sides of the elevation and we will index the bubbles in ascending order in the direction of outlet to inlet. We will retain the two bubble sizes that were used in Fig. 7 and introduce a third bubble of size $r = 0.47$. The experimental time sequences in Fig. 12 show the evolution of the six initial arrangements when propagated from rest at $\mathrm{Ca} = \mu U_0^*/\sigma = 0.01$. Movies 7–12 in the Supplemental Material [27] show the evolution of the bubbles in all initial arrangements. The two initial arrangements in Figs. 12(a) and 12(b) organize into a stable three-bubble formation and, analogous to stable two-bubble formations, they are both led by the smallest bubble and their speeds are equal to the leading bubble's isolated speed. The three bubbles are arranged in order of increasing size and, therefore, increasing propagation speeds in Fig. 12(a). Thus, the bubbles can be successively slowed down by their preceding nearest neighbors. However, in Fig. 12(b), the bubbles are not arranged in order of increasing size. The leading and middle bubbles, if the trailing bubble were not present, would propagate at the leading bubble's isolated speed and, crucially, this is slower than the trailing bubble's isolated speed. Thus, the trailing bubble can be slowed down by the middle bubble.

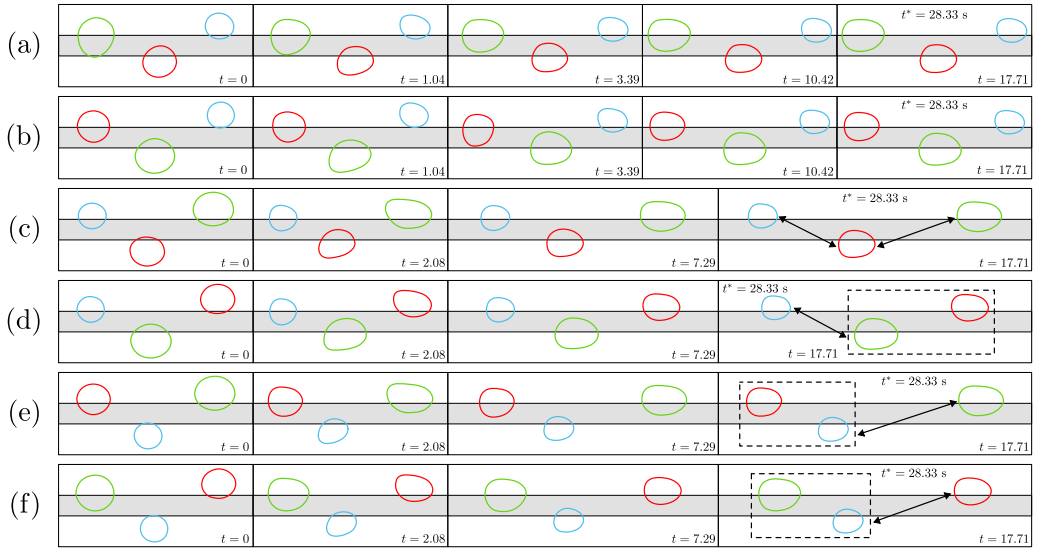

FIG. 12. Experimental time sequences that show the evolution of the six distinct arrangements of three bubbles initialized in alternation on opposite sides of the elevation when propagated from rest at Ca = $\mu U_0^*/\sigma = 0.01$. The bubble sizes are $r = 0.33$ (blue), $r = 0.40$ (red), and $r = 0.47$ (green). The two initial arrangements in (a) and (b), both of which are led by the smallest of the bubbles, organize into a stable formation of three bubbles. An arrow between a pair of bubbles in the final panels indicates that they separate indefinitely while a dashed box around a pair of bubbles indicates that they organize into a local formation of two bubbles.

The four remaining arrangements do not organize into a stable three-bubble formation and, instead, at least one pair of neighboring bubbles separates. For example, the three bubbles in Fig. 12(c) are arranged in order of decreasing size and, thus, all separate in accordance with the differences between their isolated speeds. However, in Fig. 12(d), the long-term behavior is more complex because the leading and middle bubbles organize into a stable two-bubble formation that separates from the trailing bubble.

We have overlaid the shapes of the two smallest bubbles in their stable two-bubble formation (dashed black contours) onto the stable three-bubble formations in Figs. 13(a) and 13(b). The leading bubble's shape does not change in both formations. The order of the two smallest bubbles is preserved in Fig. 13(a) and the shape of the middle bubble's front and its separation from the leading bubble's rear do not change. However, in accordance with the leading bubble's behavior in a stable two-bubble formation, its rear inclines away from the channel's centerline because of the trailing bubble's imposed flow field perturbation. The middle and trailing bubbles are interchanged

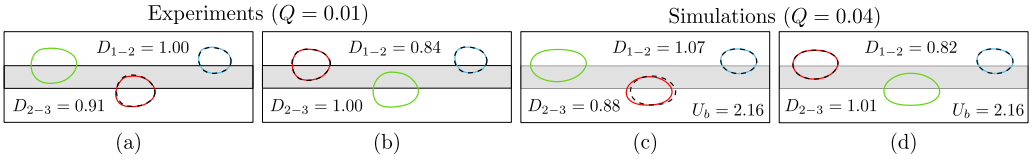

FIG. 13. The two stable formations of three bubbles that were identified in [(a), (b)] experiments at Ca = $\mu U_0^*/\sigma = 0.01$ and [(c), (d)] numerical simulations at Ca = $\mu U_0^*/\sigma = 0.04$. The bubble sizes are $r = 0.33$ (blue), $r = 0.40$ (red), and $r = 0.47$ (green). The overlaid dashed black contours are the stable two-bubble formation bubble shapes for the blue and red bubbles.

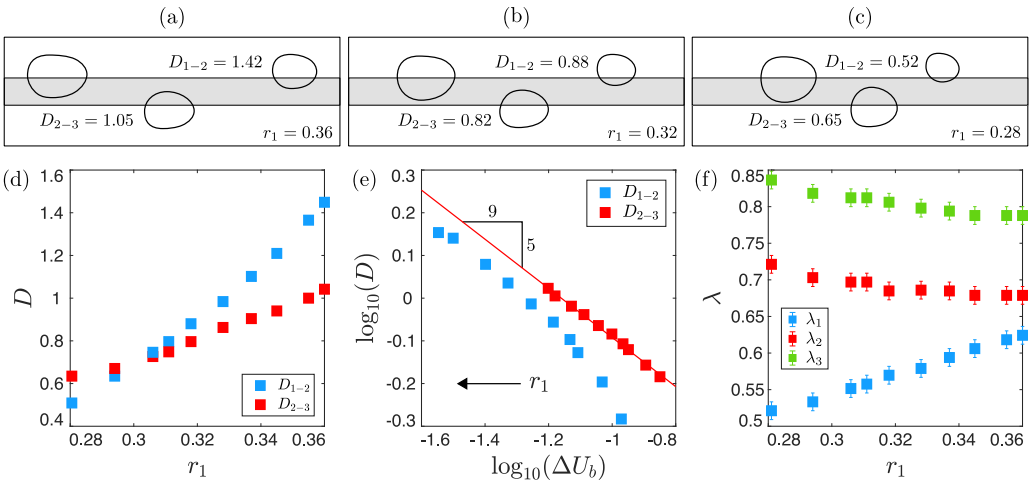

FIG. 14. [(a)–(c)] Experimental snapshots of stable three-bubble formations as leading bubble's size decreases. The bubble sizes are $r_2 = 0.40$ and $r_3 = 0.47$ and the capillary number is $\mathrm{Ca} = \mu U_0^*/\sigma = 0.01$. (d) Variation of the dimensionless separations $D_{1-2} = 2D_{1-2}^*/W^*$ and $2D_{2-3}^*/W^*$ with r_1. (e) Log-log plot of D versus ΔU_b. (f) Variation of the three bubble widths λ_1, λ_2, and λ_3 with r_1. Error bars have been omitted in (d) and (e) because they are smaller than the data markers.

in Fig. 13(b) and the value of D_{1-2} is equal to that which is obtained for a stable two-bubble formation for the same-sized bubbles [Fig. 9(b)]. The trailing bubble retains its shape from the two-bubble formation and this confirms that a bubble's shape and position within the channel's cross section are the predominant factors that influence its propagation speed. Thus, because each individual bubble's propagation speed must remain the same in order for it to remain part of the formation, the bubble shapes are only weakly influenced by their relative axial positions.

We identified qualitatively similar behavior in numerical simulations of the depth-averaged lubrication model. The two stable formations that arise from the same bubble sizes at $\mathrm{Ca} = 0.04$ are shown in Figs. 13(c) and 13(d). In agreement with the experiments, the propagation speed of both formations is marginally ($<1\%$) slower than the leading bubble's isolated propagation speed. There is a qualitative discrepancy, however, between simulations and experiments because the dimensionless separation between the leading and middle bubbles increases by 0.07 in Fig. 13(c) whereas this remained unchanged in experiments. However, this is the only qualitative discrepancy that was identified between experiments and numerical simulations.

2. Variation of the leading bubble's size

We have determined that the leading bubble exclusively sets the propagation speed of a stable formation of three bubbles. The middle and trailing bubbles adjust their shapes and overlap of the elevation in the perturbation fields of their preceding nearest neighbors in order to reduce their speeds to that of the leading bubble. We will now explore how a stable formation of three bubbles responds to a change in its propagation speed, which is imposed by varying the size of the leading bubble while the sizes of the other two bubbles and capillary number are constant.

The experimental snapshots in Figs. 14(a)–14(c) show the stable formation of three bubbles as the leading bubble's size is decreased while the middle bubble's size $r_2 = 0.40$, trailing bubble's size $r_3 = 0.47$, and capillary number $\mathrm{Ca} = 0.01$ are fixed. The bubbles become increasingly deformed (relative to their isolated states) and the separation between each pair of neighboring bubbles decreases [Fig. 14(d)]. The separation between the middle and trailing bubbles, D_{2-3}, decreases linearly on a log-log scale as the required reduction in the trailing bubble's speed ΔU_{b3}

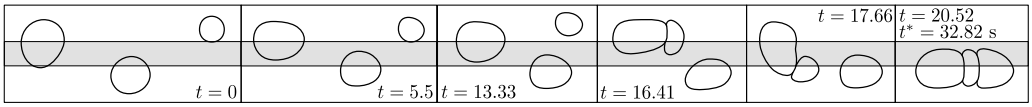

FIG. 15. Experimental time sequence showing the evolution of three bubbles of size $r_1 = 0.26$, $r_2 = 0.40$, and $r_3 = 0.47$ when propagated from rest at $\mathrm{Ca} = \mu U_0^*/\sigma = 0.01$. The leading bubble is too small to induce the necessary geometric change in the middle bubble's shape and, therefore, a stable formation of three bubbles does not exist.

increases [Fig. 14(e)], which indicates that the separation between the middle and trailing bubbles is predominantly set by the required reduction in the latter's speed. However, the separation between the leading and middle bubbles, D_{1-2}, does not exhibit this linear decrease as the required reduction in the middle bubble's speed ΔU_{b2} increases because the relative changes in the leading bubble's shape are significant. The leading bubble's width decreases significantly (by approximately 20%) as its size is decreased [Fig. 14(f)]. The decrease in the leading bubble's size will inevitably decrease the extent of its perturbation on the flow field and, thus, the middle bubble has to approach the leading bubble more closely in order to feel the required flow field perturbation that results in its necessary geometrical remodeling.

However, the bubbles do not organize into a stable formation if the leading bubble is too small. For $r_1 \leqslant 0.26$, the leading bubble is overtaken by the middle bubble following the imposition of flow (Fig. 15). The initial overtaking dynamics (i.e., in the first three panels) are qualitatively identical to the overtaking dynamics of two bubbles [Fig. 11(c)] and, thus, we infer that they are uninfluenced by the trailing bubble. The three bubbles all aggregate in a complex transient evolution and create a single compound bubble. However, as discussed previously, this state only exists transiently because liquid is expelled from the lubrication films that separates the bubbles over time and, hence, they eventually coalesce.

3. Variation of the elevation's height

We now investigate the influence of the elevation's height on a stable formation of bubbles. The influence of the elevation's height is shown for a system of three bubbles, rather than two bubbles, in order to demonstrate the global effects that it has on a stable formation of bubbles. The elevation's height was reduced to $h = 0.010$ in experiments by applying a thinner strip of PET tape along the lower glass plate and we begin by characterizing its effect on the propagation of isolated bubbles.

The isolated bubbles broaden, migrate closer to the channel's centerline, and, thus, increase their overlaps of the elevation as the elevation's height decreases [Fig. 16(a)]. The geometrical remodeling of the isolated bubble shapes reduces their propagation speeds towards those of the equivalent-sized bubbles in a uniform channel ($U_b \approx 2$) [Fig. 16(b)]. The difference between an isolated bubble's speed at the two elevation heights increases monotonically with its size because larger bubbles overlap a greater proportion of the elevation and, thus, they are increasingly affected by changes in its geometry. The isolated bubble speeds become increasingly similar (i.e., the U_b versus r curves become flatter) as the elevation's height decreases. The rate of change of U_b with r (i.e., $\mathrm{d}U_b/\mathrm{d}r$) decreases by the scale factor $K = 0.62$ as the elevation's height is reduced [Fig. 16(c)] and, thus, the value of ΔU_b between any two bubbles is multiplied by $K = 0.62$.

The experimental snapshots in Figs. 16(d) and 16(e) show the stable formation of three bubbles of sizes $r_1 = 0.33$, $r_2 = 0.40$, and $r_3 = 0.47$ at the two elevation heights. The capillary number is $\mathrm{Ca} = \mu U_0^*/\sigma = 0.04$ in both cases. The difference between the isolated bubble speeds is multiplied by $K = 0.62$ as the elevation's height decreases and, thus, the required reduction in the middle and trailing bubbles' speed decreases. The separation between neighboring pairs of bubbles at fixed capillary numbers is predominantly determined by the required reduction in their speeds (Sec. III A 1). Thus, the separation between neighboring pairs of bubbles increases as the elevation's height is reduced because the required reduction in their speeds decreases. We note that D_{1-2} and

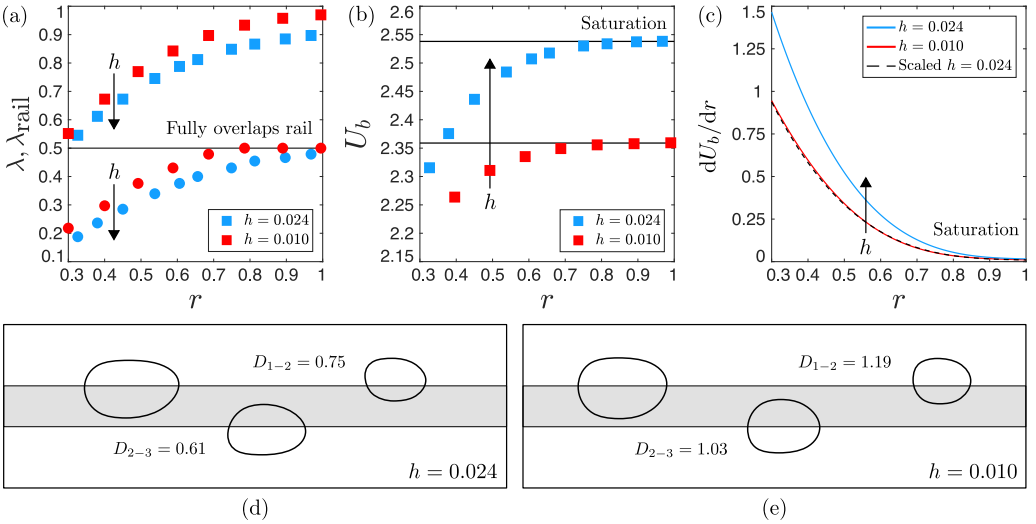

FIG. 16. (a) Variation of λ and λ_{overlap} with r for an isolated bubble at $h = 0.024$ and $h = 0.010$. (b) Variation of U_b with r for an isolated bubble at $h = 0.024$ and $h = 0.010$. (c) Variation of $\mathrm{d}U_b/\mathrm{d}r$ with r for an isolated bubble at $\mathrm{Ca} = 0.04$; these curves were obtained by differentiating power-law fits to the data points in (b). [(d), (e)] A stable three-bubble formation at (c) $h = 0.024$ and (d) $h = 0.010$ in experiments. The capillary number is $\mathrm{Ca} = 0.04$ and the bubble sizes are $r_1 = 0.33$, $r_2 = 0.40$, and $r_3 = 0.47$. Error bars have been omitted in all figures because they are smaller than the data markers.

D_{2-3} increase by approximately the same multiplicative factor because the required reduction in the middle and trailing bubbles' speeds decreases by the same scale factor and the bubble sizes are similar.

We find qualitatively identical behavior in numerical simulations of the depth-averaged lubrication model; the bubbles broaden and migrate towards the channel's centerline and the separation between neighboring bubbles increases as the elevation's height decreases [Figs. 17(a)–17(c)]. The isolated bubble speeds decrease [Fig. 17(d)] and $\mathrm{d}U_b/\mathrm{d}r$ decreases [Fig. 17(e)] by a scale factor $K < 1$ as the elevation's height decreases. The dashed black curves represent rescalings of the $h = 0.024$ curve by the scale factors. The scale factor decreases and, thus, the isolated bubble speeds become increasingly similar as the elevation's height decreases. We find that the separation between pairs of neighboring bubbles decreases near linearly with ΔU_b on a log-log scale [Fig. 17(f)], which indicates that this behavior is, indeed, predominantly driven by their isolated speeds becoming increasingly similar. The small deviation from a perfect linear relationship is attributed to the accompanying changes in the bubble shapes.

C. Larger bubble formations

1. Four-bubble formations

The fundamental design principles for stable formations of two and three bubbles are that the bubbles must be arranged in alternation on opposite sides of the elevation and the leading bubble must be the smallest and, therefore, slowest of the bubbles. We find that the same principles apply for a group of four bubbles. There are $4! = 24$ distinct initial arrangements of four bubbles lying in alternation on opposite sides of the elevation; we will retain the three bubble sizes that were used in Fig. 12 and introduce a fourth bubble of size $r = 0.54$. Figures 18(a) and 18(b) show the six stable formations that were identified in experiments and numerical simulations, respectively, at the two usual capillary numbers. Movies 13–18 in the Supplemental Material [27] show the evolution of the relevant initial configurations of bubbles towards the stable formations. The six formations

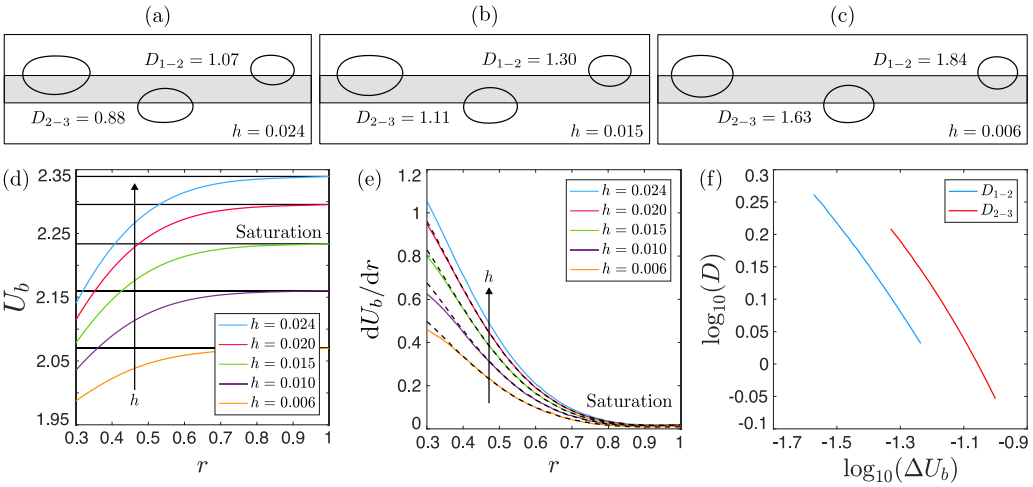

FIG. 17. [(a)–(c)] Stable three-bubble formations at various values of the elevation height h in the depth-averaged lubrication model at $\mathrm{Ca} = \mu U_0^*/\sigma = 0.04$. The bubble sizes are $r_1 = 0.33$, $r_2 = 0.40$, and $r_3 = 0.47$. (d) Variation of $U_b = U_b^*/U_0^*$ with r at different elevation heights. (e) Variation of $\mathrm{d}U_b/\mathrm{d}r$ with r at different elevation heights. The dashed black curves correspond to rescalings of the $h = 0.024$ curve by a determined scale factor K. (f) Log-log plot of D versus ΔU_b.

are all led by the smallest bubble and their speeds are equal to and marginally (<1%) slower than the leading bubble's isolated speed, respectively, in experiments and numerical simulations. Furthermore, the bubble shapes are approximately constant in all six formations and this, again, reinforces that a bubble's speed is predominantly determined by its shape and position within the channel's cross section. The remaining 18 arrangements do not organize into stable formations and, instead, they partition into subgroups of independently propagating bubbles. The subgroups, depending on the order of the bubbles, are comprised of smaller stable formations and/or single bubbles. However, for brevity, we have not included them in this paper.

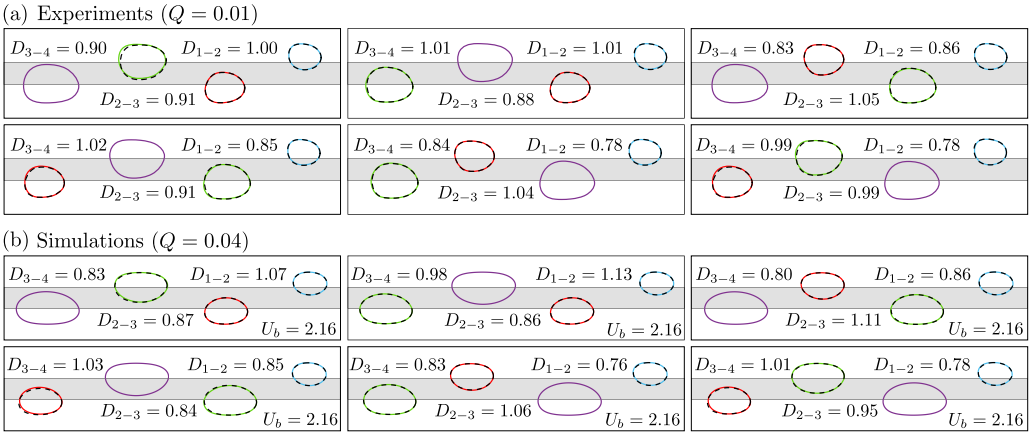

FIG. 18. The six stable four-bubble formations that were identified in (a) experiments at $\mathrm{Ca} = \mu U_0^*/\sigma = 0.01$ and (b) numerical simulations at $\mathrm{Ca} = \mu U_0^*/\sigma = 0.04$. The bubble sizes are $r = 0.33$ (blue), $r = 0.40$ (red), $r = 0.47$ (green), and $r = 0.54$ (purple). The overlaid dashed black contours are the stable three-bubble formation bubble shapes for the blue, red, and green, bubbles.

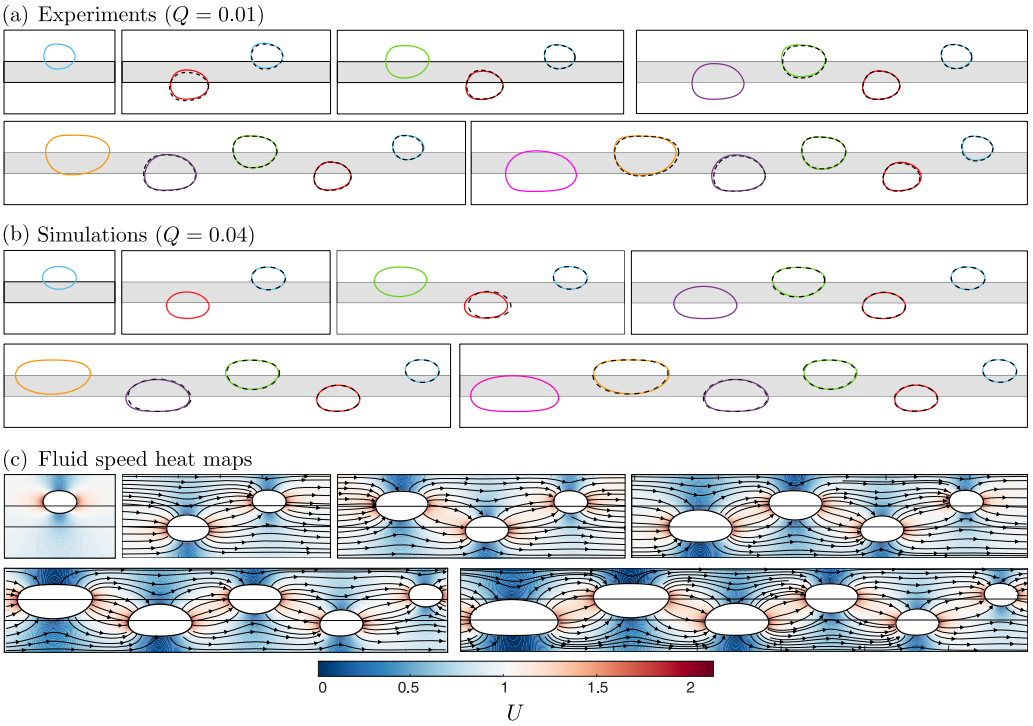

FIG. 19. The sequential process of building up to a stable formation of six bubbles in (a) experiments at $\mathrm{Ca} = \mu U_0^*/\sigma = 0.01$ and (b) numerical simulations at $\mathrm{Ca} = \mu U_0^*/\sigma = 0.04$. The experimental channel's width is $W^* = 40.0 \pm 0.1$ mm and its depth is $H^* = 1.0 \pm 0.1$ mm. The elevation's width is $w^* = 10.0 \pm 0.1$ mm and its height is $h^* = 24 \pm 1$ μm. The previous stable formation (dashed black contours) has been overlaid onto each panel. The bubble sizes are $r = 0.33$ (blue), $r = 0.40$ (red), $r = 0.47$ (green), $r = 0.54$ (purple), $r = 0.61$ (yellow), and $r = 0.68$ (magenta). (c) Streamlines of the fluid flow in the laboratory frame of reference and heat map of the dimensionless fluid speed $U = U^*/U_0^*$ in the vicinity of the bubbles.

2. Larger bubble formations

The observed behaviors suggest that any particular bubble is primarily influenced by the flow field perturbation that is imposed by its preceding nearest neighbor. Thus, the leading bubble propagates as if it were isolated because the flow field in the vicinity of its front is undisturbed by the flow field perturbations that arise from the trailing bubbles. The trailing bubbles must, therefore, be successively slowed down by a "domino effect" of the two-bubble mechanism that was described in Sec. III A in order for there to be a stable multiple-bubble state. The trailing bubbles adjust their shape and overlap of the elevation in the perturbation fields of their preceding nearest neighbors in order to reduce their speeds to that of the leading bubble. The local influence of each bubble's flow field perturbation means that the established design principles will remain unchanged when we consider the addition of more bubbles to the system and, thus, we infer that such formations can be extended indefinitely. We, therefore, expect that any arrangement of bubbles lying in alternation on opposite sides of the elevation will organize into a stable formation provided that they are led by the smallest bubble and the leading bubble's size exceeds the minimum bubble size that is capable of slowing down the fastest (i.e., $r \geqslant r_s$) bubble. We have confirmed this hypothesis up to six bubbles in experiments and numerical simulations. We have consolidated the sequential process of building up to a stable formation of six bubbles from an isolated bubble in Fig. 19. The near invariance of the bubble shapes while adding more bubbles is highlighted in each panel by overlaying the previous stable formation (dashed black contours) while the numerically computed heat maps of the fluid's speed show the adjoined perturbation fields that are formed between neighboring pairs of bubbles.

D. Bubble train dynamics

Having established the fundamental design principles of stable bubble formations, we will now proceed to discuss the expected long-term behavior of an arbitrary train of initially well-separated bubbles whose sizes exceed the minimum bubble size that is capable of slowing down the fastest (i.e., $r \geqslant r_s$) bubble. We will first consider a train of N bubbles lying entirely in alternation on opposite sides of the elevation, for which there are two distinct behaviors.

(1) The bubbles will organize into a stable formation of N bubbles if they are led by the smallest bubble.

(2) The bubbles will partition into $2 \leqslant k \leqslant N$ subgroups if they are not led by the smallest bubble. The subgroups, depending on the order of the bubbles, are comprised of smaller stable formations and/or single bubbles. The subgroups are arranged in order of increasing speed in the direction of inlet to outlet and any two consecutive subgroups will separate at a rate equal to the difference between the isolated speeds of their leading bubbles.

The transient dynamics will be considerably more complex if the bubbles do not lie entirely in alternation on opposite sides of the elevation because neighboring bubbles on the same side of the elevation are susceptible to aggregation (and, once the lubricating film that separates the two bubbles has drained, eventual coalescence) events. The resulting aggregate bubble's isolated propagation speed then increases. The leading and trailing bubbles of a stable formation can aggregate with the bubble situated ahead of and behind it, respectively, depending on their propagation speeds. The bubbles will proceed to reorganize post-aggregation in accordance with the established design principles. There are several practical difficulties (e.g., an inadequate channel length) that prevented a detailed investigation of this behavior in experiments and, similarly, numerical simulations are constrained by the finite size of the computational domain. However, based on previous results, we will proceed to infer the dynamics that would occur post-aggregation. The schematics that are provided in Fig. 20 act as visual aids in order to support the following descriptions of this more generalized case.

(1) The trailing bubble of a stable formation aggregates with the bubble situated behind it: the stable formation of bubbles will be retained because the leading bubble remains the slowest of its constituent bubbles. However, the separation between the trailing bubble and its preceding nearest neighbor will decrease because the former is larger and, thus, requires a greater reduction in its speed [Fig. 20(a)].

(2) The leading bubble of a stable formation aggregates with the bubble situated ahead of it and it remains the smallest of the formation's bubbles post-aggregation: the stable formation will be retained because the leading bubble remains the slowest of its constituent bubbles. However, the separation between all neighboring pairs of bubbles will increase because of the greater reductions that are required in all of their speeds [Fig. 20(b)].

(3) The leading bubble of a stable formation aggregates with the bubble situated ahead of it and it does not remain the smallest of the formation's bubbles post-aggregation: the formation will be destroyed because the leading bubble does not remain the slowest of its constituent bubbles and the bubbles will reorganize in accordance with the established design principles. The two most extreme examples are those in which the remaining bubbles are arranged in order of decreasing or increasing size. In the former case, they will reorganize into a smaller formation and separate from the aggregate bubble [Fig. 20(c)]. However, in the latter case, all of the bubbles will separate [Fig. 20(d)]. The remaining bubbles will reorganize into a number of smaller formations in all other cases.

In general, an arbitrary bubble train will exhibit a combination of all such behaviors and a variety of stable bubble formations will transiently appear and disappear during the system's temporal evolution before it ultimately settles in a particular long-term state comprised of various steadily propagating subgroups, organized in order of decreasing speed, that separate indefinitely.

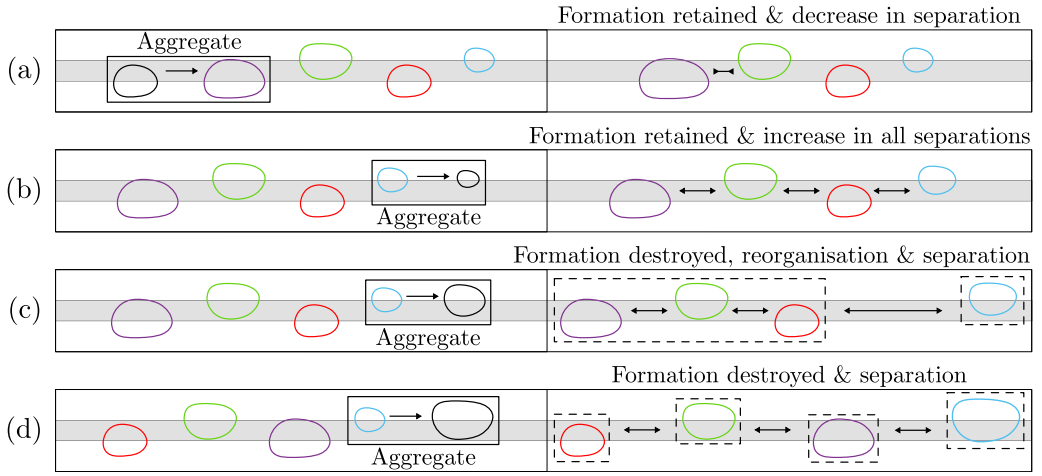

FIG. 20. Schematic diagrams of the reorganization dynamics that could occur following an aggregation event involving either the leading or trailing bubbles of a stable formation. Time increases from left to right. (a) The size of the trailing bubble increases post-aggregation. [(b)–(d)] The size of the leading bubble increases post-aggregation. Dashed boxes in the final panels indicate independently propagating formations.

IV. CONCLUDING REMARKS

We have investigated the behavior of stable multiple-bubble formations in a horizontal Hele-Shaw channel that contains an axially uniform elevation along its centerline. The presence of the elevation allows individual bubbles to propagate at different locations within the channel's cross section via the existence of stable asymmetric states and this can prevent the bubble aggregation that typically occurs in Hele-Shaw channels of uniform depth [25]. The emergence of stable multiple-bubble states is an example of complex self-organizing dynamics in a confined two-phase flow and we find that there can be multiple steadily propagating states that exist for fixed system parameters. However, in contrast, groups of polydisperse bubbles inside a Hele-Shaw channel of uniform depth will never form stable multiple-bubble states.

The constituent bubbles of a stable formation must lie in alternation on opposite sides of the elevation in order to prevent aggregation and they each propagate steadily, at the same speed, with fixed shapes. We note that Keeler *et al.* [13] found two-bubble steady states in which the bubbles were placed on the same side of the elevation or aligned along the center of the channel in the depth-averaged model. However, these states were all unstable. A stable bubble formation is always led by the smallest, which is the slowest, of its constituent bubbles. The flow field ahead of the leading bubble is undisturbed by the trailing bubbles and, hence, it propagates as if it were isolated. As a consequence, the speed of a stable formation is set by the leading bubble's isolated speed. The presence of the elevation allows reductions in speeds of the trailing bubbles to that of the leading bubble via changes in their shapes and degrees of overlap of the elevation within the perturbation fields of their preceding nearest neighbors. The extent of a bubble's shape perturbation generally increases as the difference between its isolated speed and that of the leading bubble increases. However, if the leading bubble is too small ($r_1 < 0.24$), its perturbation field cannot change the shape of the trailing bubble sufficiently to match the speed of the leading bubble and, therefore, a stable state is not possible.

The speed of each bubble is set predominantly by its shape and relative position within the channel's cross section and, furthermore, each bubble's local environment is only influenced by its nearest downstream neighbor because the spatial decay of the perturbation that is imposed by each bubble is negligible beyond one channel width. The required speed of each bubble is dictated by

the speed of the formation; this means that the trailing bubbles can be arranged in any order and their shapes are largely unaffected when they are interchanged. Thus, the number of possible stable arrangements for a group of bubbles increases factorially as the number of bubbles increases. The largest number of bubbles that we investigated was six because it becomes increasingly difficult to initialize larger groups of bubbles in experiments, and numerical simulations are constrained by the finite size of the computational domain. However, our results suggest that stable formations will exist for arbitrarily large groups of bubbles. We have established an excellent qualitative agreement between experiments and numerical simulations of a depth-averaged lubrication model. However, a degree of quantitative disagreement arises because the underlying mathematical model does not incorporate the presence of liquid films that are deposited on the upper and lower channel boundaries by the bubbles as they propagate nor does it satisfy the tangential boundary conditions and this means that, in general, bubbles in the numerical simulations propagate more slowly than those in the experiments for the same capillary number. Nevertheless, the broad agreement between our two approaches indicates that the deposited liquid films do not play a fundamental role in the stabilization of a formation of bubbles.

The fact that each bubble is influenced only by its preceding nearest neighbor means that we can understand the general behavior of an arbitrary train of bubbles of different sizes. The bubbles will, in general, undergo a variety of complex reorganizations if pairs of neighboring bubbles are situated on the same side of the elevation before they ultimately settle into a final state consisting of steadily propagating formations of bubbles that either propagate at the same speed, maintain fixed separations, or separate indefinitely when the trailing formation propagates more slowly than the leading one. The evolution towards the final state will contain considerable structure, however, because the individual bubbles will transiently organize into local formations which, depending on the order, may then interact. Although the bubbles might be expected to end up in approximate size order, the fact that the trailing bubbles in an individual formation can be arranged in any order means that the only definitive conclusion is that the smallest bubble will lead the most downstream formation of bubbles. However, in a uniform channel, small bubbles will always merge with any larger trailing bubbles until the final bubble in the train is the smallest of the remaining bubbles. Thus, the presence of the elevation allows smaller bubbles to propagate as part of the overall train, providing a more robust means of transport of polydisperse bubble trains.

The variation in the channel's depth that is provided by the elevation plays two crucial roles in this system: (i) it enables simultaneous stable, steadily propagating states for individual bubbles whose centers are not aligned with the channel's centerline and (ii) it enables an extra mechanism by which a bubble's speed can be changed because the volume of fluid displaced (and, therefore, the local viscous dissipation) can be varied without changing the bubble's shape by altering the proportion of its cross section that overlaps the elevation. However, in the absence of the elevation, the speeds of the faster bubbles cannot be altered sufficiently to form stable, steadily propagating, multiple-bubble states. As the height of the elevation decreases, the difference between the speeds of bubbles of different sizes decreases, the bubble centers move closer to the centerline of the channel, and the separation between the neighboring bubbles in a stable formation increases. We expect that the stability of the multibubble formations will be lost in the limit of a vanishing elevation height ($h^* \to 0$) because the steadily propagating asymmetric state is destroyed for individual bubbles [36]. Furthermore, we also expect that their stability will be lost in the limit of the elevation's height approaching that of the channel ($h^* \to H^*$) because, for sufficiently large elevation heights, asymmetric bubbles no longer partially overlap it and, instead, they propagate in disconnected "side channels" on opposite sides of the elevation [37]. The elevation's width is also expected to have a similar influence on the stability of multibubble formations; the elevation will tend towards a wire in the limit that its width vanishes ($w^* \to 0$) and impose a localized perturbation at the tip of a bubble similar to the experiments that are described by Zocchi *et al.* [38]. Conversely, in the limit that the elevation's width approaches that of the channel ($w^* \to W^*$), the bubbles will fully overlap it and propagate along the channel's centerline. However, we have not pursued a detailed investigation of these limits.

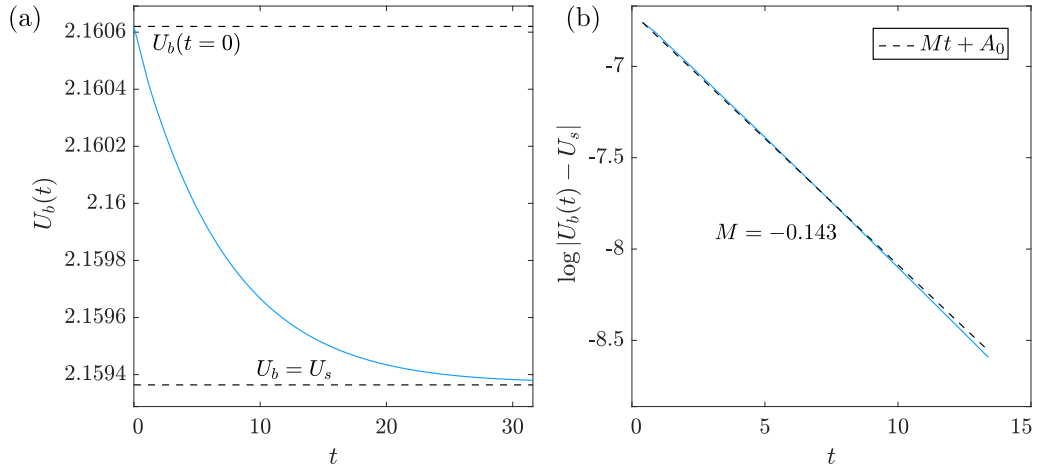

FIG. 21. (a) Evolution of the frame speed U_b after a small perturbation by the slowest-decaying eigenmode with eigenvalue -0.143. (b) Logarithmic plot of the deviation of U_b away from the steady state.

The transition from simple aggregation and separation events in a channel of uniform depth to complex dynamics involving large numbers of steadily propagating states containing multiple bubbles, simply by introducing a small perturbation to the channel's cross section, is remarkable and yet another example of geometrical perturbations eliciting complex nonlinear behaviors in spatially confined geometries. The presence of the additional steadily propagating states will slow down or even remove a number of bubble aggregation events and it may be, therefore, that such a small geometric variation could help to stabilize bubble trains propagating over long distances to slight variations in bubble sizes.

ACKNOWLEDGMENTS

This work was supported via UK Engineering and Physical Sciences Research Council (EPSRC) Grants No. EP/P026044/1 and No. EP/T008725/1 and an EPSRC DTP studentship (J.L.). J.S.K. was supported by a Leverhulme Trust Fellowship Grant No. ECF-2021-017.

APPENDIX: LINEAR STABILITY ANALYSIS

If the discretized variables representing the fluid pressure, interface position, and unknown frame speed are denoted by the composite vector $\boldsymbol{V}$ and the steady-state variables are denoted by $\boldsymbol{V}_s$, then we consider a small time-dependent perturbation to the steady state by writing

$$\boldsymbol{V} = \boldsymbol{V}_s + \varepsilon \boldsymbol{G} \mathrm{e}^{st}, \tag{A1}$$

where $\varepsilon \ll 1$, $\boldsymbol{G}$ is a discrete eigenmode, and s is the corresponding eigenvalue. At $O(\varepsilon)$, we obtain a discrete generalized eigenproblem that is highly rank deficient because time derivatives do not appear explicitly in the bulk fluid equations, and only in the kinematic boundary condition. In order to compute the eigenvalues and eigenmodes accurately and efficiently, we implement the eigensolver from the Anasazi linear algebra library that is based on Arnoldi iteration and has been used successfully in other rank-deficient generalized eigenproblems. We validate the code by comparing the most unstable eigenvalue (which corresponds to the decay rate) and the results of an initial-value problem where we use Eq. (A1) as an initial condition and measure how quickly a solution measure decays back to the steady state. Figure 21 show hows the bubble's speed, U_b, decays exponentially back to the steady state's value after perturbation. The decay rate is in excellent agreement with the slowest-decaying eigenmode with eigenvalue -0.143.

[1] L. Deike, Mass transfer at the ocean–atmosphere interface: The role of wave breaking, droplets, and bubbles, Annu. Rev. Fluid Mech. **54**, 191 (2022).
[2] A. Namiki, E. Lev, J. Birnbaum, and J. Baur, An experimental model of unconfined bubbly lava flows: Importance of localized bubble distribution, J. Geophys. Res.: Solid Earth **127**, e2022JB024139 (2022).
[3] X.-X. Xu, Study on oil–water two-phase flow in horizontal pipelines, J. Pet. Sci. Eng. **59**, 43 (2007).
[4] T. Maxworthy, Bubble formation, motion and interaction in a Hele-Shaw cell, J. Fluid Mech. **173**, 95 (1986).
[5] S. G. Huisman, P. Ern, and V. Roig, Interaction and coalescence of large bubbles rising in a thin gap, Phys. Rev. E **85**, 027302 (2012).
[6] A. Filella, P. Ern, and V. Roig, Oscillatory motion and wake of a bubble rising in a thin-gap cell, J. Fluid Mech. **778**, 60 (2015).
[7] A. Filella, P. Ern, and V. Roig, Interaction of two oscillating bubbles rising in a thin-gap cell: Vertical entrainment and interaction with vortices, J. Fluid Mech. **888**, A13 (2020).
[8] E. Bouche, V. Roig, F. Risso, and A.-M. Billet, Homogeneous swarm of high-Reynolds-number bubbles rising within a thin gap. Part 1. Bubble dynamics, J. Fluid Mech. **704**, 211 (2012).
[9] J. Ruiz-Rus, P. Ern, V. Roig, and C. Martínez-Bazán, Coalescence of bubbles in a high Reynolds number confined swarm, J. Fluid Mech. **944**, A13 (2022).
[10] B. Shen, M. Leman, M. Reyssat, and B. Tabeling, Dynamics of a small number of droplets in microfluidic Hele-Shaw cells, Exp. Fluids **55**, 1728 (2014).
[11] J. Keeler, A. Thompson, G. Lemoult, A. Hazel, and A. Juel, The influence of invariant solutions on the transient behaviour of an air bubble in a Hele-Shaw channel, Proc. R. Soc. A **475**, 20190434 (2019).
[12] A. Gaillard, J. Keeler, G. Le Lay, G. Lemoult, A. Thompson, A. Hazel, and A. Juel, The life and fate of a bubble in a geometrically perturbed Hele-Shaw channel, J. Fluid Mech. **914**, A34 (2021).
[13] J. S. Keeler, A. Gaillard, J. Lawless, A. B. Thompson, A. Juel, and A. L. Hazel, The interaction of multiple bubbles in a Hele-Shaw channel, J. Fluid Mech. **946**, A40 (2022).
[14] J. Lawless, J. Keeler, A. Gaillard, A. L. Hazel, and A. Juel, The unpredictable nature of bubble evolution, Sci. Rep. **12**, 20752 (2022).
[15] M. Gomez, D. E. Moulton, and D. Vella, Passive control of viscous flow via elastic snap-through, Phys. Rev. Lett. **119**, 144502 (2017).
[16] S. L. Anna, Droplets and bubbles in microfluidic devices, Annu. Rev. Fluid Mech. **48**, 285 (2016).
[17] U. D. Schiller, J. Fleury, R. Seemann, and G. Gompper, Collective waves in dense and confined microfluidic droplet arrays, Soft Matter **11**, 5850 (2015).
[18] K. Schirrmann, G. Caceres, and A. Juel, Self-assembly of coated microdroplets at the sudden expansion of a microchannel, Microfluid. Nanofluid. **25**, 29 (2021).
[19] B. Shen, J. Ricouvier, F. Malloggi, and P. Tabeling, Designing colloidal molecules with microfluidics, Adv. Sci. **3**, 1600012 (2016).
[20] P. Parthiban, P. S. Doyle, and M. Hashimoto, Self-assembly of droplets in three-dimensional microchannels, Soft Matter **15**, 4244 (2019).
[21] T. Beatus, T. Tlusty, and R. Bar-Ziv, Phonons in a one-dimensional microfluidic crystal, Nat. Phys. **2**, 743 (2006).
[22] T. Beatus, R. Bar-Ziv, and T. Tlusty, The physics of 2D microfluidic droplet ensembles, Phys. Rep. **516**, 103 (2012).
[23] D. Booth, I. Griffiths, and P. Howell, Circular bubbles in a Hele-Shaw channel: A Hele-Shaw Newton's cradle, J. Fluid Mech. **954**, A21 (2023).
[24] A. B. Thompson, A. L. Hazel, and A. Juel, Multiple finger propagation modes in Hele-Shaw channels of variable depth, J. Fluid Mech. **746**, 123 (2014).
[25] A. Franco-Gómez, A. B. Thompson, A. L. Hazel, and A. Juel, Bubble propagation in Hele-Shaw channels with centred constrictions, Fluid Dyn. Res. **50**, 021403 (2018).
[26] S. Tanveer and P. G. Saffman, Stability of bubbles in a Hele-Shaw cell, Phys. Fluids **30**, 2624 (1987).
[27] See Supplemental Material at http://link.aps.org/supplemental/10.1103/PhysRevFluids.9.093605 for supplemental videos.

[28] O. Reynolds, On the theory of lubrication and its application to Mr. Beauchamp tower's experiments, including an experimental determination of the viscosity of olive oil, Philos. Trans. R. Soc. London **177**, 157 (1886).
[29] M. Heil and A. L. Hazel, oomph-lib – an object-oriented multi-physics finite-element library, in *Fluid-Structure Interaction*, Lecture Notes in Computational Science and Engineering, Vol. 53, edited by H.-J. Bungartz and M. Schäfer (Springer, Berlin, 2006), pp. 19–49.
[30] C. Green and G. L. Vasconcelos, Multiple steadily translating bubbles in a Hele-Shaw channel, Proc. R. Soc. A **470**, 20130698 (2014).
[31] D. Pihler-Puzović, G. G. Peng, J. R. Lister, M. Heil, and A. Juel, Viscous fingering in a radial elastic-walled Hele-Shaw cell, J. Fluid Mech. **849**, 163 (2018).
[32] J. Fontana, A. A. Juel, N. Bergemann, M. Heil, and A. Hazel, Modelling finger propagation in elasto-rigid channels, J. Fluid Mech. **916**, A27 (2021).
[33] J. Fernandez, P. Kurowski, L. Limat, and P. Petitjeans, Wavelength selection of fingering instability inside Hele-Shaw cells, Phys. Fluids **13**, 3120 (2001).
[34] O. A. Logvinov, O. E. Ivashnyov, and N. N. Smirnov, Evaluation of viscous fingers width in Hele-Shaw flows, Acta Astronaut. **67**, 53 (2010).
[35] M. Nagel and F. Gallaire, A new prediction of wavelength selection in radial viscous fingering involving normal and tangential stresses, Phys. Fluids **25**, 124107 (2013).
[36] A. Franco-Gomez, A. Thompson, A. Hazel, and A. Juel, Sensitivity of Saffman-Taylor fingers to channel-depth perturbations, J. Fluid Mech. **794**, 343 (2016).
[37] A. L. Hazel, M. Pailha, S. J. Cox, and A. Juel, Multiple states of finger propagation in partially occluded tubes, Phys. Fluids **25**, 062106 (2013).
[38] G. Zocchi, B. E. Shaw, A. Libchaber, and L. P. Kadanoff, Finger narrowing under local perturbations in the Saffman-Taylor problem, Phys. Rev. A **36**, 1894 (1987).